DESY 09-225 ISSN 0418-9833
December 2009

Inelastic Production of J/ψ Mesons in Photoproduction and Deep Inelastic Scattering at HERA

H1 Collaboration

Abstract

A measurement is presented of inelastic photo- and electroproduction of J/ψ mesons in ep scattering at HERA. The data were recorded with the H1 detector in the period from 2004 to 2007. Single and double differential cross sections are determined and the helicity distributions of the J/ψ mesons are analysed. The results are compared to theoretical predictions in the colour singlet model and in the framework of non-relativistic QCD. Calculations in the colour singlet model using a k_T factorisation ansatz are able to give a good description of the data, while colour singlet model calculations to next-to-leading order in collinear factorisation underestimate the data.

Submitted to *Eur. Phys. J.* **C**

F.D. Aaron[5,49], C. Alexa[5], V. Andreev[25], B. Antunovic[11], S. Backovic[30], A. Baghdasaryan[38], E. Barrelet[29], W. Bartel[11], K. Begzsuren[35], A. Belousov[25], J.C. Bizot[27], V. Boudry[28], I. Bozovic-Jelisavcic[2], J. Bracinik[3], G. Brandt[11], M. Brinkmann[12,51], V. Brisson[27], D. Bruncko[16], A. Bunyatyan[13,38], G. Buschhorn[26], L. Bystritskaya[24], A.J. Campbell[11], K.B. Cantun Avila[22], K. Cerny[32], V. Cerny[16,47], V. Chekelian[26], A. Cholewa[11], J.G. Contreras[22], J.A. Coughlan[6], G. Cozzika[10], J. Cvach[31], J.B. Dainton[18], K. Daum[37,43], M. Deák[11], B. Delcourt[27], J. Delvax[4], E.A. De Wolf[4], C. Diaconu[21], V. Dodonov[13], A. Dossanov[26], A. Dubak[30,46], G. Eckerlin[11], V. Efremenko[24], S. Egli[36], A. Eliseev[25], E. Elsen[11], A. Falkiewicz[7], L. Favart[4], A. Fedotov[24], R. Felst[11], J. Feltesse[10,48], J. Ferencei[16], D.-J. Fischer[11], M. Fleischer[11], A. Fomenko[25], E. Gabathuler[18], J. Gayler[11], S. Ghazaryan[11], A. Glazov[11], L. Goerlich[7], N. Gogitidze[25], M. Gouzevitch[11], C. Grab[40], A. Grebenyuk[11], T. Greenshaw[18], B.R. Grell[11], G. Grindhammer[26], S. Habib[12], D. Haidt[11], C. Helebrant[11], R.C.W. Henderson[17], E. Hennekemper[15], H. Henschel[39], M. Herbst[15], G. Herrera[23], M. Hildebrandt[36], K.H. Hiller[39], D. Hoffmann[21], R. Horisberger[36], T. Hreus[4,44], M. Jacquet[27], X. Janssen[4], L. Jönsson[20], A.W. Jung[15], H. Jung[11,4], M. Kapichine[9], J. Katzy[11], I.R. Kenyon[3], C. Kiesling[26], M. Klein[18], C. Kleinwort[11], T. Kluge[18], A. Knutsson[11], R. Kogler[26], P. Kostka[39], M. Kraemer[11], K. Krastev[11], J. Kretzschmar[18], A. Kropivnitskaya[24], K. Krüger[15], K. Kutak[11], M.P.J. Landon[19], W. Lange[39], G. Laštovička-Medin[30], P. Laycock[18], A. Lebedev[25], V. Lendermann[15], S. Levonian[11], G. Li[27], K. Lipka[11,51], A. Liptaj[26], B. List[12], J. List[11], N. Loktionova[25], R. Lopez-Fernandez[23], V. Lubimov[24], A. Makankine[9], E. Malinovski[25], P. Marage[4], Ll. Marti[11], H.-U. Martyn[1], S.J. Maxfield[18], A. Mehta[18], A.B. Meyer[11], H. Meyer[37], J. Meyer[11], S. Mikocki[7], I. Milcewicz-Mika[7], F. Moreau[28], A. Morozov[9], J.V. Morris[6], M.U. Mozer[4], M. Mudrinic[2], K. Müller[41], P. Murín[16,44], Th. Naumann[39], P.R. Newman[3], C. Niebuhr[11], A. Nikiforov[11], D. Nikitin[9], G. Nowak[7], K. Nowak[41], J.E. Olsson[11], S. Osman[20], D. Ozerov[24], P. Pahl[11], V. Palichik[9], I. Panagoulias[l,11,42], M. Pandurovic[2], Th. Papadopoulou[l,11,42], C. Pascaud[27], G.D. Patel[18], E. Perez[10,45], A. Petrukhin[24], I. Picuric[30], S. Piec[39], D. Pitzl[11], R. Plačakytė[11], B. Pokorny[32], R. Polifka[32], B. Povh[13], V. Radescu[14], N. Raicevic[30], A. Raspiareza[26], T. Ravdandorj[35], P. Reimer[31], E. Rizvi[19], P. Robmann[41], R. Roosen[4], A. Rostovtsev[24], M. Rotaru[5], J.E. Ruiz Tabasco[22], S. Rusakov[25], D. Šálek[32], D.P.C. Sankey[6], M. Sauter[14], E. Sauvan[21], S. Schmitt[11], L. Schoeffel[10], A. Schöning[14], H.-C. Schultz-Coulon[15], F. Sefkow[11], R.N. Shaw-West[3], L.N. Shtarkov[25], S. Shushkevich[26], T. Sloan[17], I. Smiljanic[2], Y. Soloviev[25], P. Sopicki[7], D. South[8], V. Spaskov[9], A. Specka[28], Z. Staykova[11], M. Steder[11], B. Stella[33], G. Stoicea[5], U. Straumann[41], D. Sunar[11], T. Sykora[4], G. Thompson[19], P.D. Thompson[3], T. Toll[12], F. Tomasz[16], T.H. Tran[27], D. Traynor[19], P. Truöl[41], I. Tsakov[34], B. Tseepeldorj[35,50], J. Turnau[7], K. Urban[15], A. Valkárová[32], C. Vallée[21], P. Van Mechelen[4], A. Vargas Trevino[11], Y. Vazdik[25], V. Volchinski[38], M. von den Driesch[11], D. Wegener[8], Ch. Wissing[11], E. Wünsch[11], J. Žáček[32], J. Zálešák[31], Z. Zhang[27], A. Zhokin[24], T. Zimmermann[40], H. Zohrabyan[38], and F. Zomer[27]

[1] *I. Physikalisches Institut der RWTH, Aachen, Germany*
[2] *Vinca Institute of Nuclear Sciences, Belgrade, Serbia*
[3] *School of Physics and Astronomy, University of Birmingham, Birmingham, UK[b]*
[4] *Inter-University Institute for High Energies ULB-VUB, Brussels and Universiteit Antwerpen, Antwerpen, Belgium[c]*
[5] *National Institute for Physics and Nuclear Engineering (NIPNE) , Bucharest, Romania*
[6] *Rutherford Appleton Laboratory, Chilton, Didcot, UK[b]*
[7] *Institute for Nuclear Physics, Cracow, Poland[d]*
[8] *Institut für Physik, TU Dortmund, Dortmund, Germany[a]*
[9] *Joint Institute for Nuclear Research, Dubna, Russia*

[10] *CEA, DSM/Irfu, CE-Saclay, Gif-sur-Yvette, France*
[11] *DESY, Hamburg, Germany*
[12] *Institut für Experimentalphysik, Universität Hamburg, Hamburg, Germany*[a]
[13] *Max-Planck-Institut für Kernphysik, Heidelberg, Germany*
[14] *Physikalisches Institut, Universität Heidelberg, Heidelberg, Germany*[a]
[15] *Kirchhoff-Institut für Physik, Universität Heidelberg, Heidelberg, Germany*[a]
[16] *Institute of Experimental Physics, Slovak Academy of Sciences, Košice, Slovak Republic*[f]
[17] *Department of Physics, University of Lancaster, Lancaster, UK*[b]
[18] *Department of Physics, University of Liverpool, Liverpool, UK*[b]
[19] *Queen Mary and Westfield College, London, UK*[b]
[20] *Physics Department, University of Lund, Lund, Sweden*[g]
[21] *CPPM, Aix-Marseille Université, CNRS/IN2P3, Marseille, France*
[22] *Departamento de Fisica Aplicada, CINVESTAV, Mérida, Yucatán, México*[j]
[23] *Departamento de Fisica, CINVESTAV IPN, México City, México*[j]
[24] *Institute for Theoretical and Experimental Physics, Moscow, Russia*[k]
[25] *Lebedev Physical Institute, Moscow, Russia*[e]
[26] *Max-Planck-Institut für Physik, München, Germany*
[27] *LAL, Université Paris-Sud, CNRS/IN2P3, Orsay, France*
[28] *LLR, Ecole Polytechnique, CNRS/IN2P3, Palaiseau, France*
[29] *LPNHE, Université Pierre et Marie Curie Paris 6, Université Denis Diderot Paris 7, CNRS/IN2P3, Paris, France*
[30] *Faculty of Science, University of Montenegro, Podgorica, Montenegro*[e]
[31] *Institute of Physics, Academy of Sciences of the Czech Republic, Praha, Czech Republic*[h]
[32] *Faculty of Mathematics and Physics, Charles University, Praha, Czech Republic*[h]
[33] *Dipartimento di Fisica Università di Roma Tre and INFN Roma 3, Roma, Italy*
[34] *Institute for Nuclear Research and Nuclear Energy, Sofia, Bulgaria*[e]
[35] *Institute of Physics and Technology of the Mongolian Academy of Sciences, Ulaanbaatar, Mongolia*
[36] *Paul Scherrer Institut, Villigen, Switzerland*
[37] *Fachbereich C, Universität Wuppertal, Wuppertal, Germany*
[38] *Yerevan Physics Institute, Yerevan, Armenia*
[39] *DESY, Zeuthen, Germany*
[40] *Institut für Teilchenphysik, ETH, Zürich, Switzerland*[i]
[41] *Physik-Institut der Universität Zürich, Zürich, Switzerland*[i]

[42] *Also at Physics Department, National Technical University, Zografou Campus, GR-15773 Athens, Greece*
[43] *Also at Rechenzentrum, Universität Wuppertal, Wuppertal, Germany*
[44] *Also at University of P.J. Šafárik, Košice, Slovak Republic*
[45] *Also at CERN, Geneva, Switzerland*
[46] *Also at Max-Planck-Institut für Physik, München, Germany*
[47] *Also at Comenius University, Bratislava, Slovak Republic*
[48] *Also at DESY and University Hamburg, Helmholtz Humboldt Research Award*
[49] *Also at Faculty of Physics, University of Bucharest, Bucharest, Romania*
[50] *Also at Ulaanbaatar University, Ulaanbaatar, Mongolia*

[51] *Supported by the Initiative and Networking Fund of the Helmholtz Association (HGF) under the contract VH-NG-401.*

[a] *Supported by the Bundesministerium für Bildung und Forschung, FRG, under contract numbers 05H09GUF, 05H09VHC, 05H09VHF, 05H16PEA*
[b] *Supported by the UK Science and Technology Facilities Council, and formerly by the UK Particle Physics and Astronomy Research Council*
[c] *Supported by FNRS-FWO-Vlaanderen, IISN-IIKW and IWT and by Interuniversity Attraction Poles Programme, Belgian Science Policy*
[d] *Partially Supported by Polish Ministry of Science and Higher Education, grant PBS/DESY/70/2006*
[e] *Supported by the Deutsche Forschungsgemeinschaft*
[f] *Supported by VEGA SR grant no. 2/7062/ 27*
[g] *Supported by the Swedish Natural Science Research Council*
[h] *Supported by the Ministry of Education of the Czech Republic under the projects LC527, INGO-1P05LA259 and MSM0021620859*
[i] *Supported by the Swiss National Science Foundation*
[j] *Supported by CONACYT, México, grant 48778-F*
[k] *Russian Foundation for Basic Research (RFBR), grant no 1329.2008.2*
[l] *This project is co-funded by the European Social Fund (75%) and National Resources (25%) - (EPEAEK II) - PYTHAGORAS II*

1 Introduction

The description of the process of charmonium production in interactions of photons and hadrons is a challenge to theory, since it involves both the production of the heavy quark system and the formation of the bound state. Charmonium production in electron[1]-proton collisions at HERA is dominated by photon-gluon fusion: a photon emitted from the incoming electron interacts with a gluon from the proton to produce a $c\bar{c}$ pair that evolves into a charmonium state. In the colour singlet model, only those states with the same quantum numbers as the resulting charmonium contribute to the formation of a bound $c\bar{c}$ state. This is achieved by radiating a hard gluon in a perturbative process. In the factorisation ansatz of non-relativistic quantum chromodynamics, also colour octet $c\bar{c}$ states contribute to the charmonium production cross section via soft gluon radiation.

Previous measurements in electroproduction (ep) and photoproduction (γp) at HERA [1–7] are not described by predictions in the colour singlet model to leading order. In contrast, the calculation of photoproduction cross sections to next-to-leading order (NLO) [8] showed a reasonable description of the photoproduction cross sections. The calculation proved that the corrections with respect to leading order results are very large, increasing towards large transverse momentum of the J/ψ meson. The same calculation, repeated recently with an up-to-date set of theoretical parameters [9], results in a prediction which is about a factor of three below the measured cross sections, indicating that corrections beyond NLO are needed and/or that contributions from colour octet states may be sizable.

In this paper a measurement is presented of inelastic J/ψ meson production at HERA. The measurement uses a larger data sample than previous results [1–4] and benefits from improved systematics. The data sets were collected in the years 2004 to 2007 with the H1 detector. The J/ψ meson candidates are identified by the leptonic decay into two muons or electrons. The cross sections are measured for both electroproduction and photoproduction. For the photoproduction sample J/ψ meson polarisation variables are determined. The data samples are restricted to the region of phase space where contributions from diffractive charmonium production are suppressed.

2 Theoretical Models

In order to describe inelastic charmonium production in the framework of perturbative QCD different models have been proposed, such as the colour-evaporation model [10, 11], the colour-singlet model (CSM) [12–16], the factorisation ansatz in non-relativistic quantum chromodynamics (NRQCD) [17–19] and soft colour interactions [20]. In this paper the most recent calculations using the CSM or NRQCD are compared to the data.

In the CSM, only charm quark pairs in a colour singlet state with the same quantum numbers as the resulting charmonium contribute to the formation of a bound $c\bar{c}$ state. This is achieved by radiating a hard gluon in the perturbative process. The factorisation ansatz in NRQCD includes also colour octet $c\bar{c}$ states in the charmonium production cross section. The size of

[1] In this paper "electron" is used to denote both electron and positron.

these colour octet contributions, described by long distance matrix elements (LDME), is defined by additional free parameters which were determined in fits to the Tevatron data [21]. The NRQCD factorisation approach contains also the colour singlet model which is recovered in the limit in which the colour-octet LDME tend to zero.

The following calculations are compared to the measurements presented in this paper:

- A calculation of J/ψ meson photoproduction via a colour singlet mechanism [9] provides predictions for both cross sections and helicity distributions to next-to-leading order. The uncertainty of this calculation is estimated by variations of the charm quark mass and the factorisation and renormalisation scales.
- A calculation at NLO for photoproduction cross sections includes the full framework of NRQCD [22]. The uncertainty of this calculation is dominated by the limited knowledge of the LDMEs.
- CSM predictions in the k_T factorisation approach are employed as implemented in the MC generator CASCADE [23]. Higher order parton emissions based on the CCFM evolution equations [24] are matched to $\mathcal{O}(\alpha_s)$ matrix elements in which the incoming parton can be off-shell. The uncertainty on the calculation is estimated by varying the renormalisation scale by a factor of two. In addition polarisation variables in the k_T factorisation approach are calculated analytically [25].

Parameters and variations used in the theoretical calculations are given in table 1.

3 H1 Detector

The H1 detector is described in detail elsewhere [28]. Here only the components essential to the present analysis are briefly described. A right handed Cartesian coordinate system is used with the origin at the nominal primary ep interaction vertex. The proton beam direction defines the z axis. The polar angles θ and transverse momenta P_T of all particles are defined with respect to this axis. The azimuthal angle ϕ defines the particle direction in the transverse plane. The pseudorapidity is defined as $\eta = -\ln\tan\frac{\theta}{2}$.

Charged particles emerging from the ep interaction region are measured by the central tracking detector (CTD) in the pseudo-rapidity range $|\eta| < 1.74$. The CTD consists of two large cylindrical central jet drift chambers (CJC) which are interleaved by a z-chamber and arranged concentrically around the beam-line in a magnetic field of $1.16\ \mathrm{T}$. The CTD provides triggering information based on track segments from the CJC [29, 30], and on the z-position of the vertex from the 5-layer multi-wire proportional chamber [31] which is situated inside the inner CJC. To provide the best possible spatial track reconstruction, CTD tracks are linked to hits in the vertex detector, the central silicon tracker CST [32]. The CST is installed close to the interaction point, surrounding the beam pipe in the pseudo-rapidity range $|\eta| < 1.3$ and consists of two layers of double sided silicon strip sensors.

Charged and neutral particles are measured in the liquid argon calorimeter (LAr) [33] which surrounds the tracking chambers and covers the range $-1.5 < \eta < 3.4$ and a lead/scintillating-fibre

CSM (NLO), P. Artoisenet et al. [9]	
PDF	CTEQ6M [26]
renormalisation and factorisation scale	$\mu_0 = 4m_c$
scale variation	$0.5\mu_0 < \mu_f$, $\mu_r < 2\mu_0$ and $0.5 < \mu_r/\mu_f < 2$
CS LDME	$\langle \mathcal{O}\,[\underline{1},^3 S_1]\rangle = 1.16\,\mathrm{GeV}^3$
m_c	$1.4 < m_c < 1.6\,\mathrm{GeV}$
$\alpha_s(M_Z)$	0.118 (+ running at 2 loops)
NRQCD (NLO), M. Butenschön et al. [22]	
PDF	CTEQ6M [26]
renormalisation and factorisation scale	$\mu_0 = \sqrt{4m_c^2 + P_{T,\psi}^2}$
NRQCD scale	$\mu_\Lambda = m_c$
m_c	$m_{J/\psi}/2 \approx 1.55\,\mathrm{GeV}$
$\alpha_s(M_Z)$	0.1176 ± 0.002
CSM (k_T factorisation), CASCADE [23]	
PDF	CCFM set A0 [27] ('set A0$^{\pm}$' for μ_r uncertainties)
renormalisation scale	$\mu_0 = \sqrt{m_\psi^2 + P_{T,\psi}^2}$
renormalisation scale variation	$0.5\mu_0 < \mu_r < 2\mu_0$
factorisation scale	$\sqrt{\hat{s} + Q_\perp^2}$
m_c	$1.5\,\mathrm{GeV}$
$\Lambda^{(3)}_{\mathrm{QCD}}$	$200\,\mathrm{MeV}$
CSM (k_T factorisation), S. Baranov [25]	
PDF	CCFM set A0 [27]
renormalisation and factorisation scale	$\mu_0 = \sqrt{m_\psi^2 + P_{T,\psi}^2}$
m_c	$1.5\,\mathrm{GeV}$
$\Lambda^{(3)}_{\mathrm{QCD}}$	$200\,\mathrm{MeV}$

Table 1: Summary of the parameters employed in the CSM and NRQCD calculations used to compare to the measurements in this paper. In this table PDF means parton distribution function of the proton, $\hat{s}$ denotes the invariant mass square of the hard subprocess and $Q_\perp$ the initial transverse momentum of the partonic system (γg).

calorimeter SpaCal [34], covering the backward region $-4.0 < \eta < -1.4$. The calorimeters are surrounded by the solenoidal magnet and the iron return yoke. The yoke is instrumented with 16 layers of limited streamer tubes, forming the central muon detector (CMD) in the range $-2.5 < \eta < 3.4$.

The luminosity determination is based on the measurement of the Bethe-Heitler process $ep \to ep\gamma$, where the photon is detected in a calorimeter located downstream of the interaction point in the electron beam direction at $z = -104\,\mathrm{m}$.

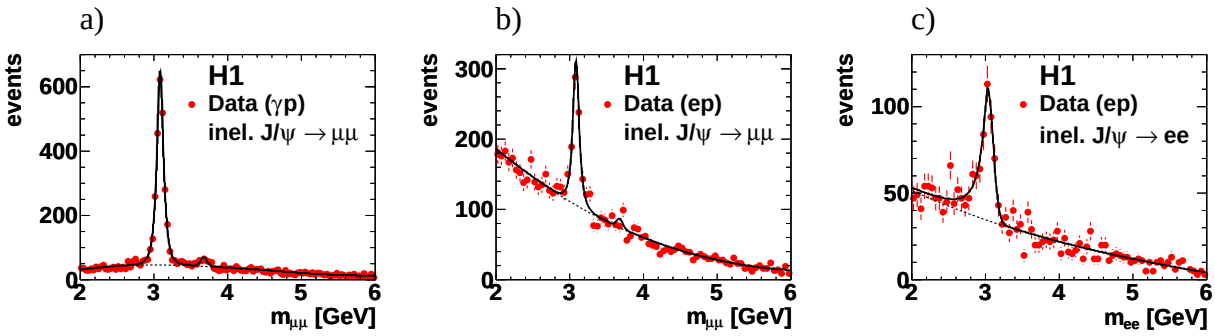

Figure 1: Invariant mass spectra of two oppositely charged leptons after all selection cuts for a) the photoproduction (γp) sample and b,c) the electroproduction (ep) samples as listed in table 2. The lines show the results of fits to signals and backgrounds.

4 Data Analysis

The kinematics of inelastic charmonium production at HERA are described using the following variables: the square of the ep centre of mass energy $s = (p + k)^2$, where p and k denote the four vectors of electron and proton respectively; the negative squared four momentum transfer $Q^2 = -q^2$, where q is the four vector of the virtual photon; and the mass of the hadronic final state $W_{\gamma p} = \sqrt{(p+q)^2}$. $W_{\gamma p}$ is related to the scaled energy transfer $y = (p \cdot q)/(p \cdot k)$ via ${W_{\gamma p}}^2 = ys - Q^2$. In addition, the elasticity of the J/ψ meson production process is defined as $z = (p_\psi \cdot p)/(q \cdot p)$, where p_ψ is the four momentum of the J/ψ meson. The elasticity denotes the fractional energy of the photon transferred to the J/ψ meson in the proton rest system.

Events are selected separately in the photoproduction and electroproduction regimes. Photoproduction events are selected by requiring that no isolated high energy electromagnetic cluster, consistent with a signal from a scattered electron, is detected in the calorimeters. This limits the virtuality to values of $Q^2 \lesssim 2.5\,\mathrm{GeV}^2$, resulting in a mean value of $\langle Q^2 \rangle \approx 0.085\,\mathrm{GeV}^2$. Conversely, for the electroproduction sample, a scattered electron with energy of more than $10\,\mathrm{GeV}$ is required to be reconstructed in the backward calorimeter (SpaCal), corresponding to a range in photon virtuality $3.6 < Q^2 < 100\,\mathrm{GeV}^2$.

In this analysis the photon virtuality Q^2 is reconstructed from the scattered electron energy E'_e and polar angle θ'_e as $Q^2 = 4E_eE'_e\cos^2(\theta'_e/2)$, where E_e denotes the energy of the beam electron. The variable y is reconstructed using the relation $y = \sum_h(E - p_z)/2E_e$ for photoproduction [35] and $y = \sum_h(E - p_z)/\sum(E - p_z)$ for electroproduction [36]. The sums in the numerator include all particles of the hadronic final state without the scattered electron, which is only included in the sum of the denominator for electroproduction. The elasticity z is then obtained from $z = (E - p_z)_{J/\psi}/\sum_h(E - p_z)$, where $(E - p_z)_{J/\psi}$ is calculated from the decay particles of the J/ψ meson. The kinematics of the final state particles are obtained from charged particle tracks reconstructed in the CTD and energy depositions in the LAr and SpaCal calorimeters [37, 38].

The J/ψ meson candidates are reconstructed through their decays into two oppositely charged muons or electrons. These decay leptons are reconstructed as charged particles in the CTD

	Photoproduction	Electroproduction	
	$J/\psi \to \mu^+\mu^-$	$J/\psi \to \mu^+\mu^-$	$J/\psi \to e^+e^-$
kinematic range			
	$Q^2 < 2.5\,\mathrm{GeV}^2$	$3.6 < Q^2 < 100\,\mathrm{GeV}^2$	
	$60\ \mathrm{GeV} < W_{\gamma p} < 240\ \mathrm{GeV}$		
	$P_{T,\psi} > 1\,\mathrm{GeV}$	$P^*_{T,\psi} > 1\,\mathrm{GeV}$	
	$0.3 < z < 0.9$		
event selection			
	$P_{T,\ell} > 800\,\mathrm{MeV}$		
	$20^\circ < \theta_\mu < 160^\circ$	$20^\circ < \theta_\mu < 160^\circ$	$20^\circ < \theta_e < 150^\circ$
	$\mathrm{N_{Trk}} \geq 5$ (in the range $20^\circ < \theta < 160^\circ$)		
event samples			
$N_{J/\psi}$	2320 ± 54	501 ± 34	290 ± 24
$\mathcal{L}_{int}$	$165\,\mathrm{pb}^{-1}$	$315\,\mathrm{pb}^{-1}$	$315\,\mathrm{pb}^{-1}$

Table 2: List of selection cuts and event yields for each of the three data samples.

with a transverse momentum of at least $800\,\mathrm{MeV}$. Muon candidates are identified as minimum ionising particles in the LAr calorimeter or through track segments in the CMD ($20^\circ < \theta_\mu < 160^\circ$) [39]. Electron candidates are identified through their energy deposit in the central calorimeter ($20^\circ < \theta_e < 150^\circ$) [40]. For trigger reasons the photoproduction sample of J/ψ meson events is restricted to decays into $\mu^+\mu^-$, while the electroproduction sample includes both leptonic decay channels. The photoproduction sample was recorded in the years 2006 and 2007 and corresponds to an integrated luminosity of $\mathcal{L} = 165\,\mathrm{pb}^{-1}$, while the electroproduction sample was recorded in the years 2004 to 2007 and corresponds to an integrated luminosity of $\mathcal{L} = 315\,\mathrm{pb}^{-1}$.

The measurement is performed in the kinematic range $60 < W_{\gamma p} < 240\,\mathrm{GeV}$, $0.3 < z < 0.9$ and $P_{T,\psi}(P^*_{T,\psi}) > 1\,\mathrm{GeV}$. In photoproduction the transverse momentum $P_{T,\psi}$ is measured in the lab frame, while in electroproduction the transverse momentum $P^*_{T,\psi}$ is calculated in the $\gamma^* p$ rest frame. To suppress contributions from diffractive production of J/ψ and $\psi(2S)$ mesons, selected events are required to contain at least five reconstructed tracks in the central region of the detector ($20^\circ < \theta < 160^\circ$). The reconstruction efficiency accounts for this experimental cut and the measured cross sections are corrected for this track multiplicity cut.

Figure 1 shows the invariant mass spectra of the leptons in the selected event samples. The number of signal events, $N_{J/\psi}$, is obtained in all bins of the cross section measurements from a fit to the mass distributions in the interval $2 < m_{\ell\ell} < 6$ GeV. For the decay into muons the signal peak is described using a modified Gaussian [7]. In the case of a decay into two electrons an exponential is added to the lower mass region of the signal Gaussian in order to account for the radiative tail [39]. For the differential cross section measurements, the width and asymmetry term of the mass peak in each bin are fixed to the values obtained from the full samples. For both decay channels, the background is parametrised by a polynomial of third

order. At $m_{\ell\ell} \approx 3.7\,\mathrm{GeV}$, the nominal mass of $\psi(2S)$ mesons, an additional Gaussian with fixed position and width is allowed in all analysis bins.

The selection criteria and the obtained event samples are summarised in table 2.

5 Monte Carlo Simulations

Cross sections and polarisation parameters are derived by correcting the measured number of events and angular distributions for detector effects, such as detector resolutions and inefficiencies. Several Monte Carlo generator programs are used to determine the corrections. All samples are passed through a detailed simulation of the H1 detector response based on the GEANT program [43] and through the same reconstruction and analysis algorithms as used for the data.

Signal events are generated using the Monte Carlo generator CASCADE [23]. Elastic and proton-dissociative production of $\psi(2S)$ mesons is simulated using DIFFVM [44] with parameters tuned to describe the results of previous H1 measurements [45, 46]. The Monte Carlo generator PYTHIA [47] is used for the description of the contribution from b hadron decays as described in section 6. All generators use the JETSET part of the PYTHIA program [47] to simulate the hadronisation and decay processes.

Signal events as simulated with the Monte Carlo generator CASCADE are compared with the data after final selection in figures 2 and 3. All data distributions in these figures are corrected for contributions from non-resonant background events using a sideband method described in [39].

Corrections as a function of $W_{\gamma p}$ and $P_{T,\psi}$ in bins of the elasticity z are applied to the CASCADE Monte Carlo simulation in order to describe the data. Details of the procedure are described in [39]. In figure 2 distributions for the photoproduction sample are compared to CASCADE Monte Carlo predictions before and after correction for the observables $P_{T,\mu}$, θ_μ, $P_{T,\psi}$, θ_ψ, $W_{\gamma p}$ and z. Similarly, in figure 3, the summed distributions for the two electroproduction samples ($J/\psi \to \mu^+\mu^-$ and $J/\psi \to e^+e^-$) are shown for the observables $P^*_{T,\psi}$, θ_ψ, Q^2, $\Sigma P_{T,\mathrm{charged}}$, $W_{\gamma p}$ and z. Here, $\Sigma P_{T,\mathrm{charged}}$ is the scalar sum over the transverse momenta of all measured charged particles except for the scattered electron and the J/ψ meson decay leptons. The corrected CASCADE simulation gives a good description of all aspects of the data and is used to correct the data for losses due to limited acceptance and efficiency of the detector.

6 Backgrounds

Remaining backgrounds to prompt J/ψ meson production in the selected sample originate from feed-down processes, i.e. J/ψ mesons produced in decays of diffractively or inelastically produced $\psi(2S)$ mesons and χ_c mesons or of b hadrons.

Inelastic production of $\psi(2S)$ mesons with a subsequent decay into J/ψ mesons is expected to contribute about $15 - 20\,\%$ to the selected J/ψ meson samples [8, 48]. Since the production

processes are the same, the inelastic $\psi(2S)$ mesons show similar dependences on the kinematic variables.

Diffractive production of $\psi(2S)$ mesons contributes at large values of z by decays into a J/ψ meson and two charged pions. These events typically contain three or four reconstructed charged tracks in the central detector ($20^\circ < \theta < 160^\circ$). In figure 4a) the distribution of the charged track multiplicity measured in the central detector is shown for the photoproduction sample selected using all selection criteria given in table 2 except for the track multiplicity cut, which is relaxed to $\mathrm{N_{Trk}} \geq 3$. The data are described by the sum of the CASCADE simulation and the prediction for diffractive $\psi(2S)$ production, as simulated using the DIFFVM Monte Carlo generator. In the final selection remaining contributions from diffractive $\psi(2S)$ meson production amount to about 1.3% in the total sample and to about 5% in the highest elasticity bin, $0.75 < z < 0.9$.

The fraction of events arising from b hadrons decaying into $J/\psi + X$ is estimated using the PYTHIA simulation. The PYTHIA prediction is scaled by a factor of 2, based on results from previous measurements of beauty production at HERA [49, 50]. This scaled prediction by PYTHIA amounts to 5% in the total sample and about 20% in the lowest z bin. It is confirmed within uncertainties by the following determination using data. The fraction of events in the photoproduction sample containing b hadrons is estimated using the impact parameter of the decay muons to exploit the lifetime signature of b hadrons. The impact parameter, δ, of the decay muon tracks is defined as the distance of closest approach in the transverse plane to the reconstructed primary vertex. The sign of the impact parameter is defined as positive if the angle between the decay muon and the J/ψ meson momentum direction is less than $90\,^\circ$, and is defined as negative otherwise. A signed significance $\mathcal{S} = \delta/\sigma(\delta)$ is reconstructed by weighting the reconstructed signed impact parameter with its uncertainty [51]. Figure 4b) shows the distribution of the signed significance for events in the interval $0.3 < z < 0.4$. The histogram is filled with the signed significance of the decay muons for all events where both muon tracks have at least one hit in the CST. The fraction of events coming from the decay of b hadrons is obtained from a fit of the significance distribution of CASCADE (simulating prompt J/ψ meson production) plus PYTHIA (simulating $b\bar{b}$ events with subsequent decays into J/ψ + X) to that of the data. The fit results are dominated by the region of small signed significances, $\mathcal{S} < 3$, due to large statistical uncertainties at larger values of $\mathcal{S}$. The distribution of the data is corrected for non-resonant contributions using the side bands [39]. The relative contribution from b hadrons as resulting from the fits are shown in figure 4c) for three bins of z. The scaled predictions from PYTHIA are found to be in good agreement with the measured fractions, indicating that the background from b hadrons is under control.

The contribution from χ_c production and decay was studied [3] and found negligibly small in the present kinematic region, $0.3 < z < 0.9$.

7 Systematic Uncertainties

The sources of systematic uncertainties of the cross section measurement are listed in table 3 and are detailed in the following:

Source	Uncertainty [%]		
	Photoproduction	Electroproduction	
	$J/\psi \to \mu^+\mu^-$	$J/\psi \to \mu^+\mu^-$	$J/\psi \to e^+e^-$
Decay leptons reconstruction	1	1	2
Decay leptons identification	3	3	3
Number of signal events	2	2	4
Trigger	3	2	2
Scattered electron energy scale	—	2	2
Hadronic final state energy scale	4	3	3
Integrated luminosity	4	3.2	3.2
Model uncertainties	5	5	5
Decay branching ratio	1	1	1
Sum	9.0	8.2	9.1

Table 3: Systematic uncertainties of the J/ψ meson production cross section. The total systematic uncertainty is the sum of the contributions added in quadrature.

- The uncertainty on the cross section due to the track and vertex reconstruction efficiency has been determined to be $1\,\%$ for $J/\psi \to \mu\mu$ and $2\,\%$ for $J/\psi \to ee$.

- The efficiency for the identification of the leptons is determined using a high statistics sample of events of elastically produced J/ψ mesons [39]. The detector simulation is reweighted to match the efficiency measured in the data as necessary. Remaining differences are smaller than $3\,\%$ everywhere and are taken as systematic uncertainty.

- The systematic uncertainty on the determination of the number of signal events, obtained by a fit to the mass distributions in every analysis bin, is determined by a variation of the extraction method. Comparing the number of signal events for binned and unbinned log-likelihood fits yields a systematic uncertainty of $0.5\,\%$. In addition, the result from the fit to background and signal is compared to the number of signal events above the fitted background function in the mass window between 2.95 and $3.2\,\mathrm{GeV}$. An uncertainty of $2\,\%$ for the decay into muons and $4\,\%$ for the electrons is found. The uncertainty for the electron is larger due to an additional uncertainty originating from the description of the radiative tail.

- The trigger efficiencies are determined using independent trigger channels. For the electroproduction sample the trigger efficiency is measured to be $(97 \pm 2)\,\%$. In the photoproduction sample the trigger efficiency depends mainly on the identification of the decay muons in the central muon system. The efficiency amounts to about $70\,\%$ with a systematic uncertainty of $3\,\%$. A detailed description of the determination of the trigger efficiencies can be found in [39].

- For the electroproduction sample the measurement of the scattered electron energy is known with a scale uncertainty of $1\,\%$. The uncertainty of the scattering angle is 1 mrad. Both uncertainties combined lead to an uncertainty of the cross section measurement of $2\,\%$ on average.

- The hadronic energy scale uncertainty is $4\,\%$ in the LAr and $7\,\%$ in the SpaCal. This leads to an uncertainty on the cross sections measurement of $3\,\%$ for the electroproduction sample and $4\,\%$ for the photoproduction sample.
- The integrated luminosity is known to a precision of $3.2\,\%$ for the electroproduction sample and $4.0\,\%$ for the photoproduction sample.
- The dependence of the result on model assumptions made in the CASCADE Monte Carlo simulation were investigated and found to amount to $5\,\%$ in total. The model uncertainty arising from the knowledge of the decay angular distributions, explained in section 9, is determined by variation of the parameter α in the simulation by ± 0.3. This variation results in a change of the cross section of up to $4\,\%$. The systematic uncertainty originating from the uncertainty of the slope of the $P_{T,\psi}$ ($P^*_{T,\psi}$) distribution in the simulation is determined by a variation of this distribution as described in [39]. This variation results in a change of the cross section of up to $4\,\%$.
- The branching ratios of the leptonic decay channels of the J/ψ meson are known with an accuracy of $1\,\%$ [42].

The total systematic uncertainty is obtained by adding all the above contributions in quadrature. A total systematic uncertainty of $9\,\%$ is determined for the photoproduction sample. For the combined electroproduction cross section the total systematic uncertainty is $8.5\,\%$ The same uncertainties are attributed to all bins of the cross section measurement. For the measurement of the helicity distributions only the uncorrelated systematic uncertainties are taken into account. They amount to about $3.5\,\%$ and are negligible compared to the statistical uncertainties.

8 Cross Section Measurements

The cross section measurement is performed in the kinematic range $60 < W_{\gamma p} < 240\,\mathrm{GeV}$, $0.3 < z < 0.9$ and $P_{T,\psi}(P^*_{T,\psi}) > 1\,\mathrm{GeV}$. The photon virtuality Q^2 is limited in the electroproduction analysis to $3.6 < Q^2 < 100\,\mathrm{GeV}^2$ and for the photoproduction sample to $Q^2 < 2.5\,\mathrm{GeV}^2$.

For the measurement of differential cross sections the number of signal events in each bin is corrected for detector inefficiencies and acceptance and normalised to integrated luminosity and branching ratio. They are not corrected for QED radiative effects. The electroproduction cross sections, measured from $J/\psi \to \mu\mu$ and $J/\psi \to ee$, are combined [39]. The differential cross sections are bin-centre corrected using MC simulations. In order to avoid model dependencies, the measured cross sections are not corrected for contributions from backgrounds as described in section 6. All measured cross sections are listed in tables 4 – 9 together with statistical and systematic uncertainties.

For the photoproduction sample the measured ep cross sections are transformed to γp cross sections using the photon flux factors presented in table 5, calculated in the Weizsäcker Williams approximation [52]. The differential J/ψ meson photoproduction cross section is measured as function of the elasticity z and the squared transverse momentum $P^2_{T,\psi}$ of the J/ψ meson.

The total γp cross section is measured in bins of the photon proton centre of mass energy $W_{\gamma p}$. The results are displayed in figure 5 and show a reasonable agreement with the prediction from the CASCADE MC generator. A variation of the renormalisation scale by a factor of two ($0.5\mu_0 < \mu_r < 2\mu_0$) has little effect as shown by the band in the figures. In addition to the CASCADE prediction, the remaining contributions from diffractive $\psi(2S)$ mesons and from b hadrons are shown. The distributions in $P^2_{T,\psi}$ and z are further investigated by dividing the sample into bins of $P^2_{T,\psi}$ and z, respectively as shown in figure 6. The z distribution tends to flatten off towards larger values of $P_{T,\psi}$ presented in figure 6a). It can be seen that differences between the data and the CASCADE prediction are localised at low elasticities and low transverse momenta of the J/ψ mesons, where CASCADE overshoots the data, and at large elasticities and large transverse momenta, where CASCADE is below the data. Taking into account that the measured cross section in the lowest elasticity bin includes a significant fraction of about $20\,\%$ of events originating from b hadron decays, the difference to the CASCADE prediction is even more significant.

Results for electroproduction are shown in figure 7 and figure 8. Differential ep cross sections are measured as functions of the photon virtuality Q^2, the squared transverse momentum of the J/ψ meson in the photon proton rest frame $P^{*2}_{T,\psi}$, the energy $W_{\gamma p}$ and the elasticity z. Figure 8 shows differential cross sections as a function of the elasticity z in bins of $P^*_{T,\psi}$ and as a function of $P^{*2}_{T,\psi}$ in bins of z. A comparison of the electroproduction data with predictions from the Monte Carlo generator CASCADE reveals in general a reasonable agreement with the data. Differences in shape can be seen in the differential cross section as a function of $P^{*2}_{T,\psi}$.

For photoproduction, several theory calculations to next-to-leading order have been performed and are compared with the data in figure 9. A calculation in the CSM at NLO [8] was repeated using up-to-date sets of scale parameters [9, 22], yielding predictions as shown in figure 9a)-b). The shapes of the data are reasonably described, whereas the normalisation of the prediction is about a factor three below the data, with large uncertainties, indicating that corrections beyond next-to-leading order are necessary in order to describe the data. Estimates of the NNLO contribution for charmonium production at the Tevatron [53, 54] indicate that these contributions can be large indeed.

The calculation to next-to-leading order has been extended to include colour octet contributions resulting in a larger cross section [22]. A comparison of this prediction with the data is shown in figure 9c)-d). The dominant uncertainty arises from the difference in the predicted cross section when using LO colour octet LDMEs or higher order improved LDMEs [22]. The NRQCD prediction fails however in describing the shape of the differential cross section as a function of the elasticity z, even within the presently large uncertainties of the calculation.

9 Polarisation Measurement

The measurement of the J/ψ meson helicity distributions provides an independent method to distinguish between different production mechanisms. The measurement is performed for the photoproduction data sample. The J/ψ meson polarisation is measured by analysing the decay angle distributions of the J/ψ meson, and their dependence on $P_{T,\psi}$ and z, in two complementary frames [55]: the helicity frame and the Collins-Soper frame. In the helicity frame the

polarisation axis z in the J/ψ meson rest frame is defined by the flight direction of the J/ψ meson in the γp rest frame, whereas the polarisation in the Collins-Soper frame is measured with respect to the bisector of proton ($-\vec{p_p}$) and photon ($\vec{p_\gamma}$) in the J/ψ meson rest frame [56]. Subsequently, the frame-dependent polarisation axis is taken as z axis of a right handed coordinate system, where the x and z axis lie in a plane spanned by the photon and proton directions. The y axis is perpendicular to this plane and is the same in both reference frames. The polar (θ^*) and azimuthal (ϕ^*) angles of the positive decay muons are used.

The parametrisation of the measured decay angle distributions as function of $\cos(\theta^*)$ and ϕ^* is given by [56]:

$$\frac{d\sigma}{d\cos\theta^*} \propto 1 + \alpha\cos^2\theta^*\,; \tag{1}$$

$$\frac{d\sigma}{d\phi^*} \propto 1 + \frac{\alpha}{3} + \frac{\nu}{3}\cos 2\phi^*. \tag{2}$$

The polarisation variables α and ν can be related to elements of the spin density matrix for the J/ψ meson. Moreover, $\alpha = +1$ and -1 corresponds to fully transverse and longitudinal polarisation of the J/ψ meson, respectively.

A χ^2 fit is performed in each bin of the polarisation measurement, comparing data to Monte Carlo samples on reconstruction level probing values for α and ν between -1 and $+1$. Systematic uncertainties on this measurement are negligible compared to rather large statistical uncertainties. The results for α and ν as a function of $P_{T,\psi}$ and z are presented for the helicity frame in figure 11 and in figure 12 for the Collins-Soper frame. The values for the polarisation parameters in both frames are listed in table 10.

Within uncertainties the J/ψ mesons produced inelastically at HERA are unpolarised. The measurements are compared to predictions using a k_T factorisation ansatz [25] and to calculations in the CSM in collinear factorisation at leading order [25] and next-to-leading order [9]. The predictions in the k_T factorisation ansatz describe the data. The NLO calculations show a similar trend within large uncertainties. In contrast, the leading order CSM calculation predicts larger values for the polarisation variables than the measured ones for many bins and is disfavoured by the measurement. A similar measurement was published by the ZEUS collaboration in a different kinematic range [57].

10 Conclusions

A measurement of inelastic J/ψ meson production is performed. Differential cross sections with improved statistical and systematic uncertainties are presented for both electroproduction and photoproduction. Polarisation parameters for the photoproduction of J/ψ mesons are measured in two different reference frames, the helicity frame and the Collins-Soper frame.

The data are compared to a number of recent theory predictions. It is found that predictions based on k_T factorisation in the colour singlet model are able to describe the cross sections and the helicity distributions well. Calculations based on collinear factorisation in the colour singlet model at next-to-leading order produce a reasonable description of the shape of the measured

cross sections, but are lower in normalisation. They give an acceptable description of the polarisation parameter measurements within the large uncertainties. The failure to describe the cross section measurements and the strong sensitivity to scale variations indicate that calculations beyond next-to-leading order are necessary. Moreover contributions from colour octet states may be significant.

Acknowledgements

We are grateful to the HERA machine group whose outstanding efforts have made this experiment possible. We thank the engineers and technicians for their work in constructing and maintaining the H1 detector, our funding agencies for financial support, the DESY technical staff for continual assistance and the DESY directorate for support and for the hospitality which they extend to the non-DESY members of the collaboration. We would like to thank Pierre Artoisenet, Sergey Baranov, Mathias Butenschön, Bernd Kniehl, Michael Krämer and Fabio Maltoni for providing theory calculations for this paper as well as for helpful discussions.

References

[1] S. Aid *et al.* [H1 Collaboration], Nucl. Phys. B **472** (1996) 3 [hep-ex/9603005].

[2] C. Adloff *et al.* [H1 Collaboration], Eur. Phys. J. C **10** (1999) 373 [hep-ex/9903008].

[3] C. Adloff *et al.* [H1 Collaboration], Eur. Phys. J. C **25** (2002) 25 [hep-ex/0205064].

[4] C. Adloff *et al.* [H1 Collaboration], Eur. Phys. J. C **25** (2002) 41 [hep-ex/0205065].

[5] J. Breitweg *et al.* [ZEUS Collaboration], Z. Phys. C **76** (1997) 599 [hep-ex/9708010].

[6] S. Chekanov *et al.* [ZEUS Collaboration], Eur. Phys. J. C **27** (2003) 173 [hep-ex/0211011].

[7] S. Chekanov *et al.* [ZEUS Collaboration], Eur. Phys. J. C **44** (2005) 13 [hep-ex/0505008].

[8] M. Krämer, Nucl. Phys. B **459** (1996) 3 [hep-ph/9508409].

[9] P. Artoisenet, J. M. Campbell, F. Maltoni and F. Tramontano, Phys. Rev. Lett. **102** (2009) 142001 [arXiv:0901.4352].

[10] F. Halzen, Phys. Lett. B **69** (1977) 105.

[11] O. J. P. Eboli, E. M. Gregores and F. Halzen, Phys. Lett. B **451** (1999) 241 [hep-ph/9802421].

[12] C. H. Chang, Nucl. Phys. B **172** (1980) 425.

[13] E. L. Berger and D. L. Jones, Phys. Rev. D **23** (1981) 1521.

[14] R. Baier and R. Rückl, Nucl. Phys. B **201** (1982) 1.

[15] R. Baier and R. Rückl, Phys. Lett. B **102** (1981) 364.

[16] R. Baier and R. Rückl, Z. Phys. C **19** (1983) 251.

[17] W. E. Caswell and G. P. Lepage, Phys. Lett. B **167** (1986) 437.

[18] B. A. Thacker and G. P. Lepage, Phys. Rev. D **43** (1991) 196.

[19] G. T. Bodwin, E. Braaten and G. P. Lepage, Phys. Rev. D **51** (1995) 1125 [Erratum-ibid. D **55** (1997) 5853] [hep-ph/9407339].

[20] A. Edin, G. Ingelman and J. Rathsman, Phys. Rev. D **56** (1997) 7317 [hep-ph/9705311].

[21] E. Braaten, B. A. Kniehl and J. Lee, Phys. Rev. D **62** (2000) 094005 [hep-ph/9911436].

[22] M. Butenschön and B. A. Kniehl, arXiv:0909.2798.

[23] H. Jung and G.P. Salam, Eur. Phys. J. C **19** (2001) 351 [hep-ph/0012143];
H. Jung, Comput. Phys. Commun. **143** (2002) 100 [hep-ph/0109102].

[24] M. Ciafaloni, Nucl. Phys. B **296** (1988) 49;
S. Catani, F. Fiorani and G. Marchesini, Phys. Lett. B **234** (1990) 339; *idem*, Nucl. Phys. B **336** (1990) 18;
G. Marchesini, Nucl. Phys. B **445** (1995) 49.

[25] S. P. Baranov, private communication, 2009, based on: JETP Lett. **88** (2008) 471.

[26] J. Pumplin, *et al.*, JHEP **0207** (2002) 012 [hep-ph/0201195].

[27] H. Jung, "Un-integrated PDFs in CCFM," hep-ph/0411287.

[28] I. Abt *et al.* [H1 Collaboration], Nucl. Instrum. Meth. A **386** (1997) 310 and 348.

[29] A. Baird *et al.*, IEEE Trans. Nucl. Sci. **48** (2001) 1276 [hep-ex/0104010].

[30] D. Meer *et al.*, IEEE Trans. Nucl. Sci. **49** (2002) 357 [hep-ex/0107010].

[31] J. Becker *et al.*, Nucl. Instrum. Meth. A **586** (2008) 190 [physics/0701002].

[32] D. Pitzl *et al.*, Nucl. Instrum. Meth. A **454** (2000) 334 [hep-ex/0002044];
B. List, Nucl. Instrum. Meth. A **501** (2001) 49.

[33] B. Andrieu *et al.* [H1 Calorimeter Group], Nucl. Instrum. Meth. A **336** (1993) 460.

[34] T. Nicholls *et al.* [H1 SPACAL Group], Nucl. Instrum. Meth. A **374** (1996) 149.

[35] A. Blondel and F. Jacquet, in: Proc. Study of an ep Facility for Europe (Ed. U. Amaldi), DESY 79/48, (1979) 391.

[36] U. Bassler and G. Bernardi, Nucl. Instrum. Meth. A **361** (1995) 197 [hep-ex/9412004].

[37] S. Hellwig, "Investigation of the D* - pi(slow) double tagging method in charm analyses. (In German)," diploma thesis, University of Hamburg (2004), H1 thesis 341 (available at http://www-h1.desy.de/psfiles/theses/).

[38] M. Peez, "Search for deviations from the standard model in high transverse energy processes at the electron proton collider HERA. (In French)", PhD thesis, University of Lyon (2003), H1 thesis 317 (available at http://www-h1.desy.de/psfiles/theses/).

[39] M. Steder, "Measurement of inelastic charmonium production at HERA", PhD thesis, University of Hamburg (2008), H1 thesis 488 (available at http://www-h1.desy.de/psfiles/theses/).

[40] M. Sauter, "Measurement of Beauty Photoproduction at Threshold using Di-Electron Events with the H1 Detector at HERA", PhD thesis, ETH Zürich (2009), H1 thesis 517 (available at http://www-h1.desy.de/psfiles/theses/).

[41] F. D. Aaron *et al.* [H1 Collaboration], Eur. Phys. J. C **59** (2009) 589 [arXiv:0808.1003].

[42] C. Amsler *et al.* [Particle Data Group], Phys. Lett. B **667** (2008) 1 and 2009 partial update for the 2010 edition.

[43] R. Brun *et al.*, CERN-DD/EE-84-1 (1987).

[44] B. List and A. Mastroberardino, in: Proc. of the Workshop on Monte Carlo generators for HERA physics, ed. A. T. Doyle *et al.*, DESY-PROC-1999-02 (1999) 396.

[45] C. Adloff *et al.* [H1 Collaboration], Phys. Lett. B **421** (1998) 385 [hep-ex/9711012].

[46] C. Adloff *et al.* [H1 Collaboration], Phys. Lett. B **541** (2002) 251 [hep-ex/0205107].

[47] T. Sjöstrand, Comput. Phys. Commun. **39** (1986) 347;
T. Sjöstrand and M. Bengtsson, Comput. Phys. Commun. **43** (1987) 367;
T. Sjöstrand, Comput. Phys. Commun. **82** (1994) 74;
T. Sjöstrand *et al.*, Comput. Phys. Commun. **135** (2001) 238 [hep-ph/0010017].

[48] S. Chekanov *et al.* [ZEUS Collaboration], Eur. Phys. J. C **27** (2003) 173 [hep-ex/0211011].

[49] A. Aktas *et al.* [H1 Collaboration], Eur. Phys. J. C **41** (2005) 453 [hep-ex/0502010].

[50] A. Aktas *et al.* [H1 Collaboration], Eur. Phys. J. C **47** (2006) 597 [hep-ex/0605016].

[51] F. D. Aaron *et al.* [H1 Collaboration], Eur. Phys. J. C **65** (2010) 89 [arXiv:0907.2643].

[52] V. M. Budnev, I. F. Ginzburg, G. V. Meledin and V. G. Serbo, Phys. Rept. **15** (1974) 181.

[53] J. M. Campbell, F. Maltoni and F. Tramontano, Phys. Rev. Lett. **98** (2007) 252002 [hep-ph/0703113].

[54] P. Artoisenet, J. P. Lansberg and F. Maltoni, Phys. Lett. B **653** (2007) 60 [hep-ph/0703129].

[55] P. Faccioli, C. Lourenco, J. Seixas and H. K. Wöhri, Phys. Rev. Lett. **102** (2009) 151802 [arXiv:0902.4462].

[56] M. Beneke, M. Krämer and M. Vanttinen, Phys. Rev. D **57** (1998) 4258 [hep-ph/9709376].

[57] S. Chekanov *et al.* [ZEUS Collaboration], JHEP **0912** (2009) 007 [arXiv:0906.1424].

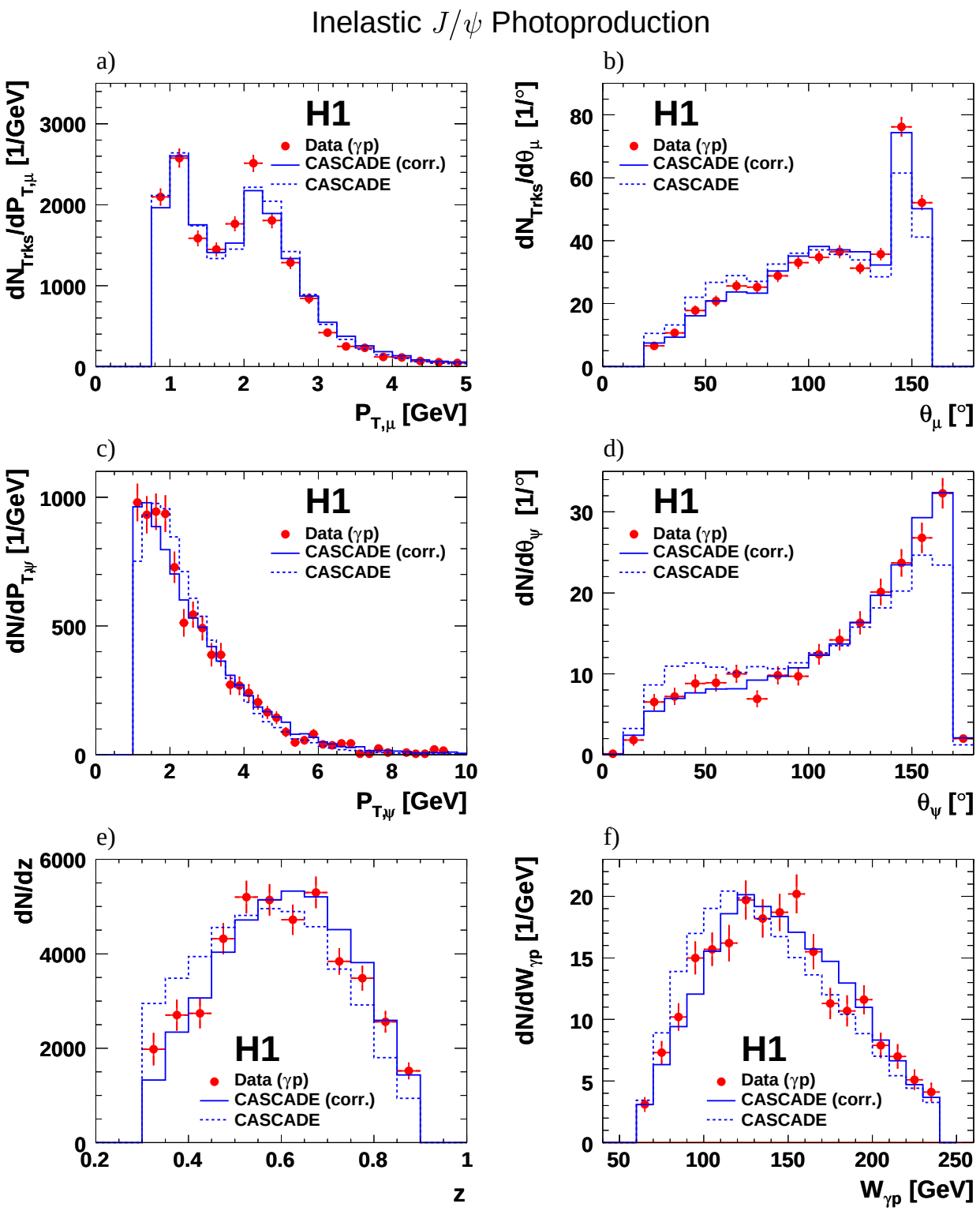

Figure 2: Control distributions of the photoproduction sample: a) the transverse momentum $P_{T,\mu}$ of the muon tracks, b) the polar angle θ_μ of the muon tracks, c) the transverse momentum $P_{T,\psi}$ of the J/ψ meson, d) the polar angle θ_ψ of the J/ψ meson, e) the elasticity z and f) the photon proton centre-of-mass energy $W_{\gamma p}$. The data are compared with predictions from the corrected CASCADE Monte Carlo simulation (solid lines), normalised to the number of entries in the data. The uncorrected CASCADE Monte Carlo prediction is shown as dashed line.

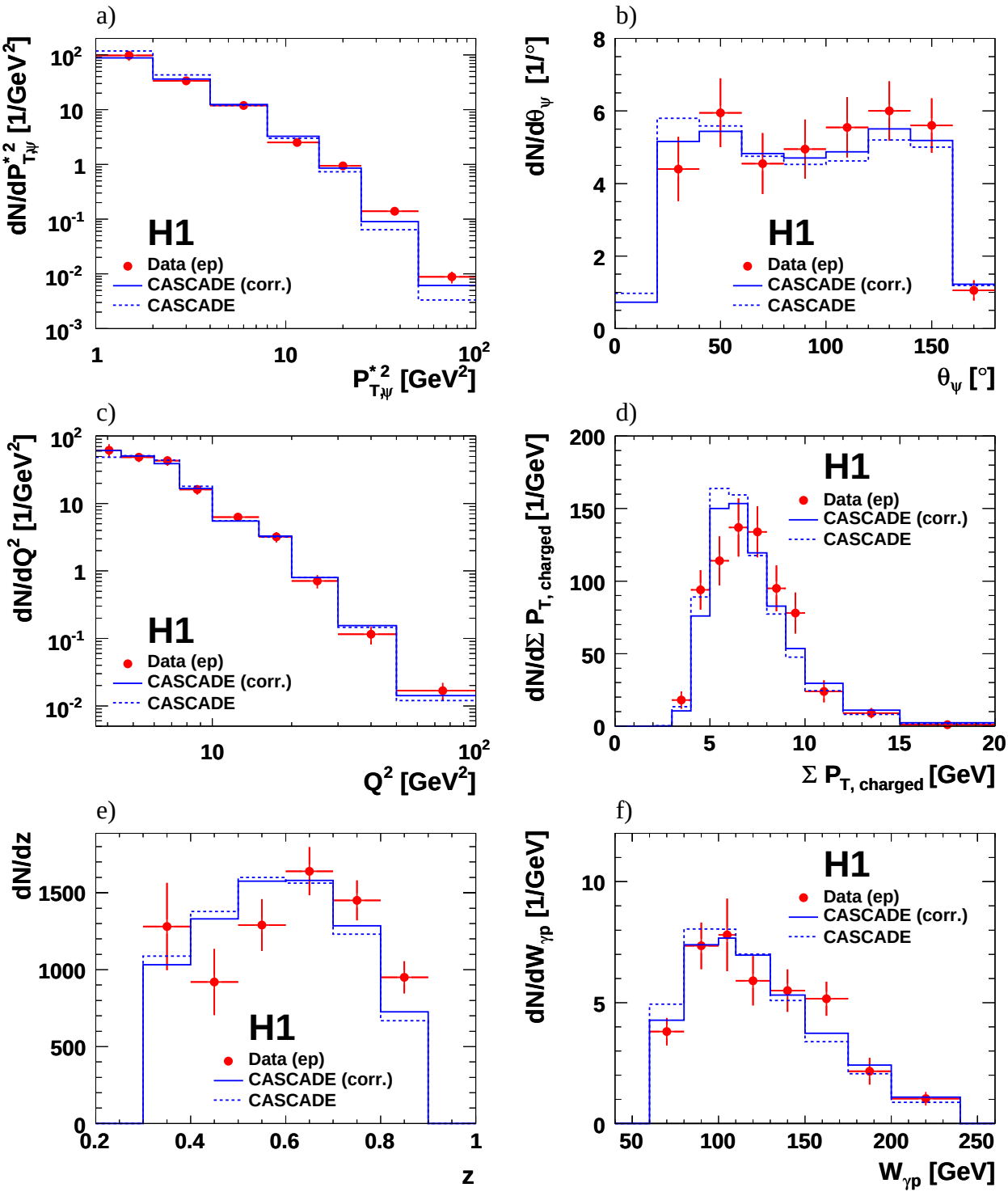

Figure 3: Control distributions of the electroproduction sample: a) The squared transverse momentum of the J/ψ meson in the photon proton rest frame $P^{*2}_{T,\psi}$, b) the polar angle of the J/ψ meson θ_ψ, c) the photon virtuality Q^2, d) the scalar transverse sum $\Sigma P_{T,\mathrm{charged}}$, e) the elasticity z and f) the photon proton centre of mass energy $W_{\gamma p}$. The data are compared with predictions from the corrected CASCADE Monte Carlo simulation (solid lines), normalised to the number of entries in the data. The uncorrected CASCADE Monte Carlo prediction is shown as dashed line.

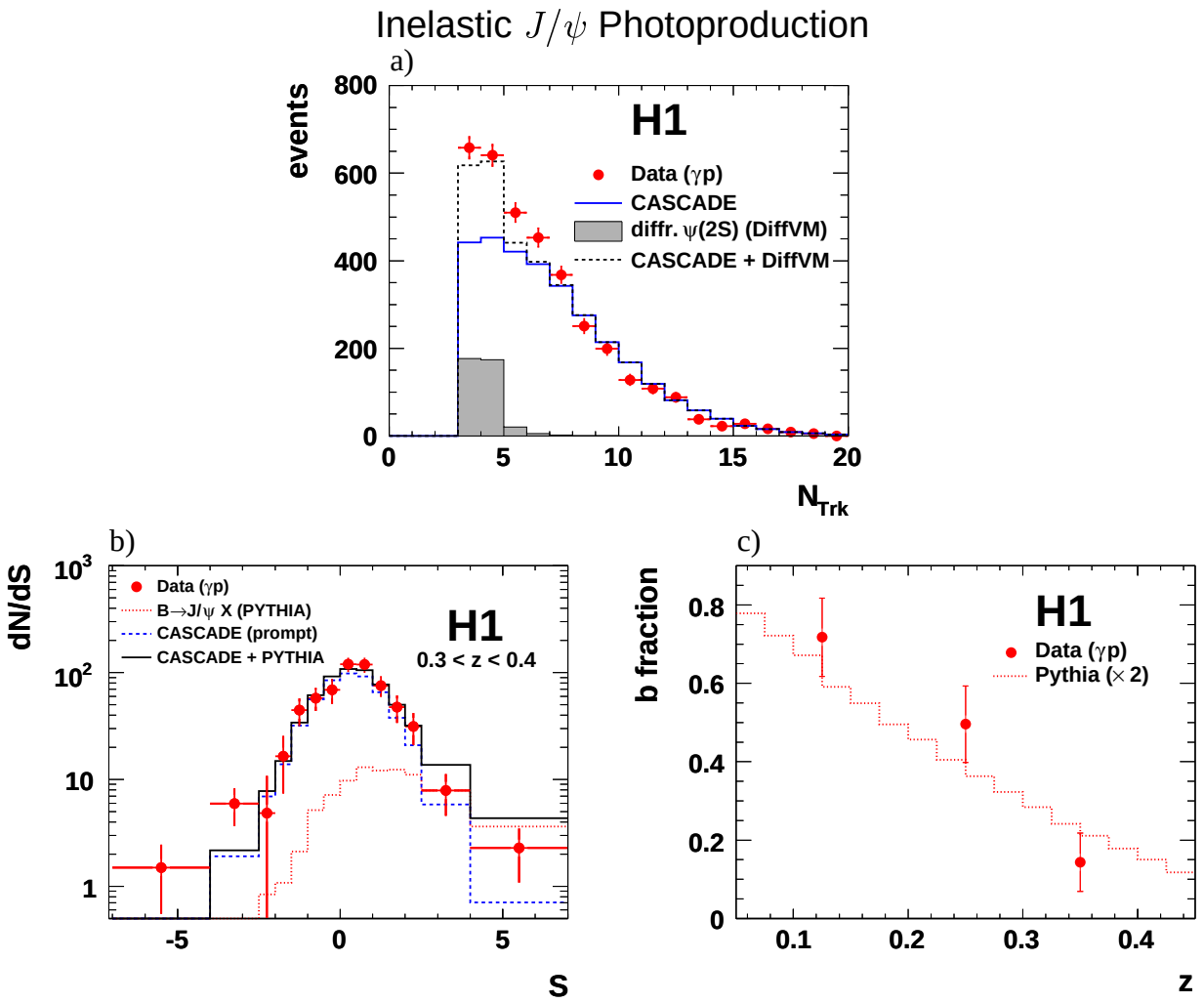

Figure 4: a) Distribution of the multiplicity of tracks, N_{Trk}, in the central region of the detector ($20^\circ < \theta < 160^\circ$) for the photoproduction sample, b) signed significance distribution $\mathcal{S}$ for the photoproduction sample at low elasticities ($0.3 < z < 0.4$) and c) measured contribution from b hadron decays for three bins of the elasticity z in comparison with the prediction based on PYTHIA (scaled up by a factor of two) and CASCADE.

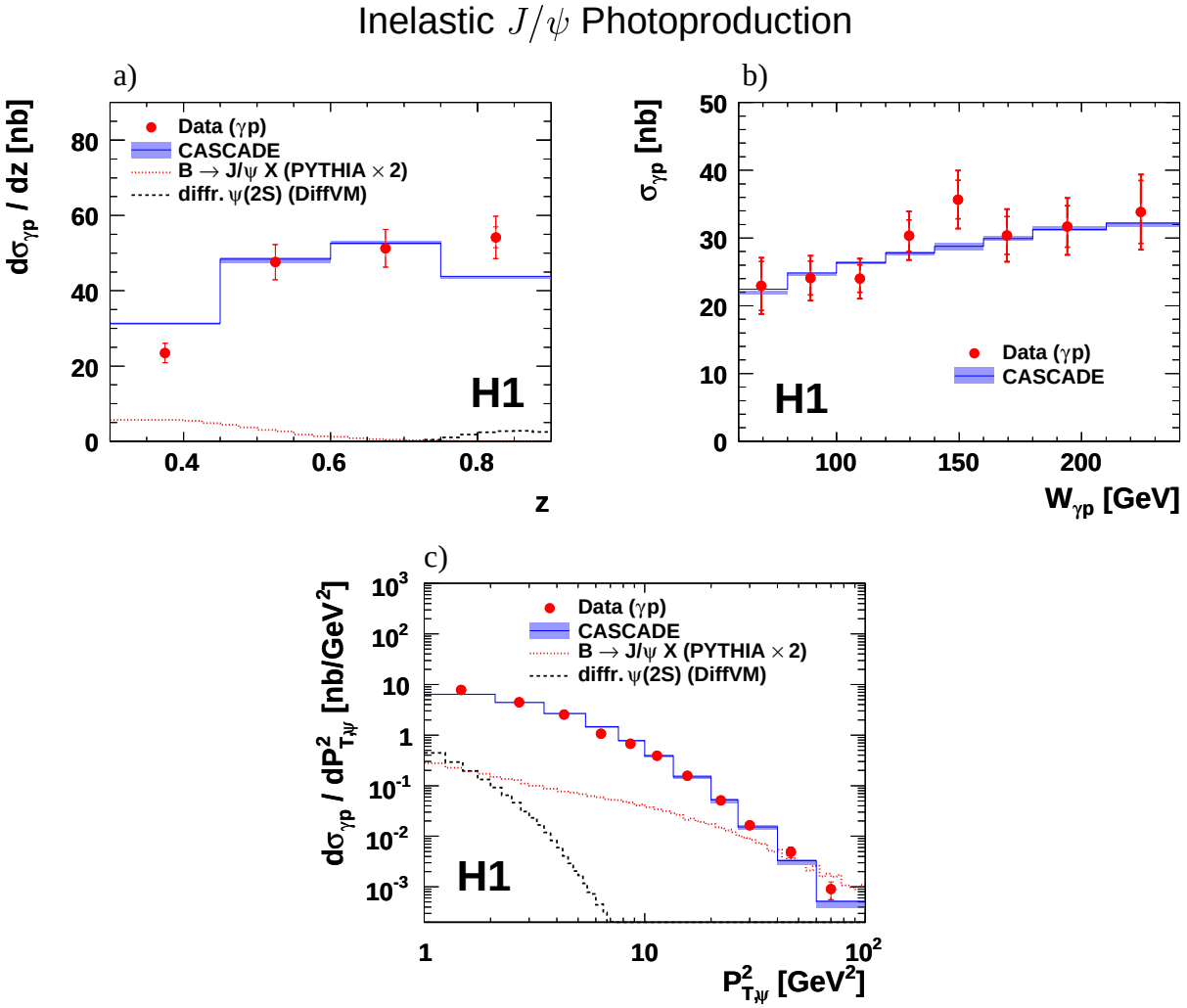

Figure 5: Differential J/ψ meson photoproduction cross sections for the kinematic range $60 < W_{\gamma p} < 240\,\mathrm{GeV}$, $0.3 < z < 0.9$ and $P_{T,\psi} > 1\,\mathrm{GeV}$, as functions of a) the elasticity z, b) the photon proton centre of mass energy $W_{\gamma p}$ and c) the squared transverse momentum of the J/ψ meson $P^2_{T,\psi}$. The inner error bar represents the statistical uncertainty and the outer error bar indicates the statistical and systematic uncertainties added in quadrature. The data are compared to the predictions from CASCADE (solid line). The uncertainty band of the CASCADE prediction arises from a scale variation by a factor of two. The dashed and dotted lines indicate the remaining background from diffractive $\psi(2S)$ or b hadron decays respectively as estimated using MC simulations.

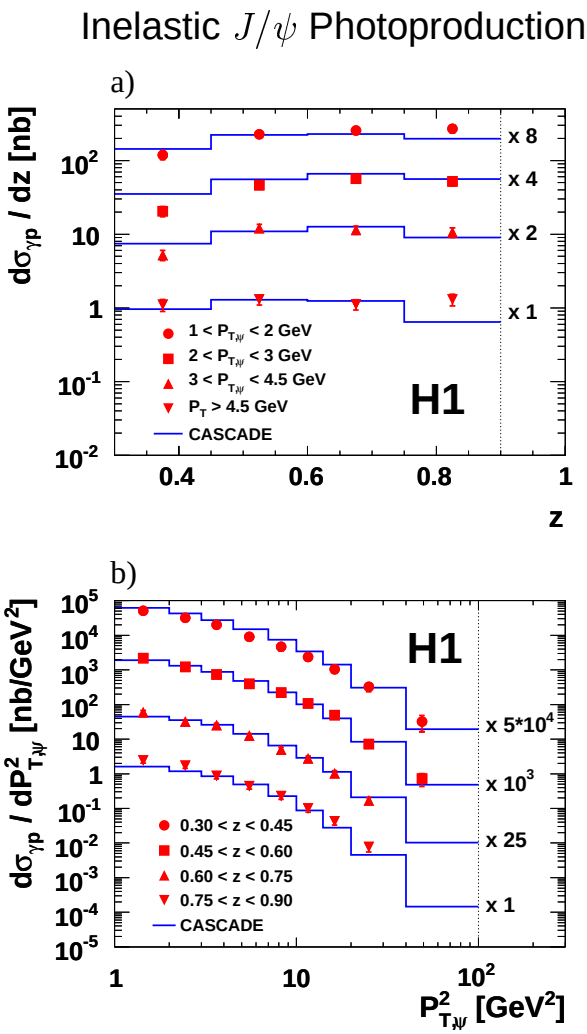

Figure 6: a) Differential J/ψ meson cross sections as a function of z in four bins of $P_{T,\psi}$ and b) differential J/ψ meson cross sections as a function of $P^2_{T,\psi}$ in four bins of z. The inner error bar represents the statistical uncertainty and the outer error bar indicates the statistical and systematic uncertainties added in quadrature. For visibility, the measured cross sections are scaled by the factors indicated in the figures. The data are compared to the predictions from CASCADE (lines).

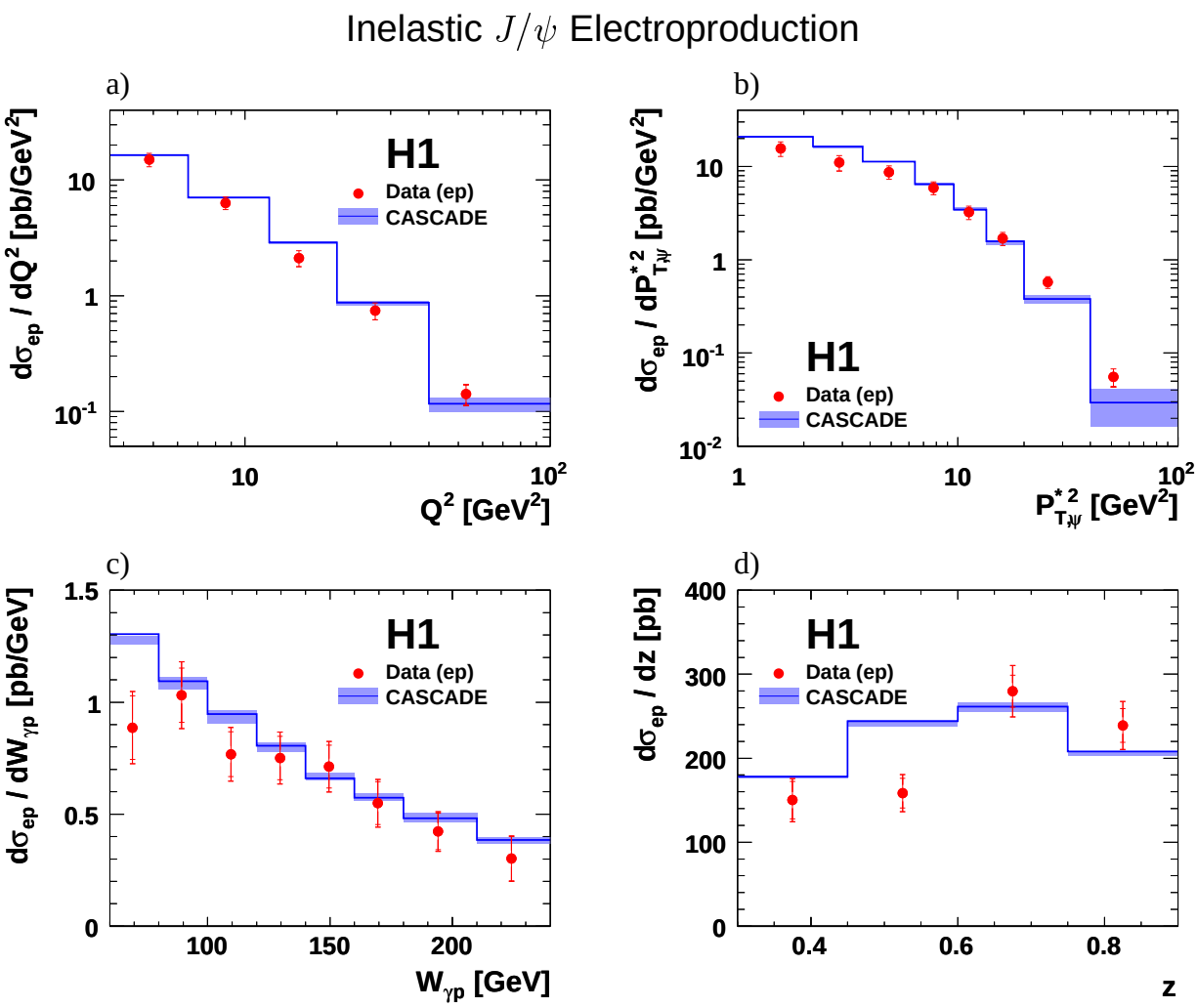

Figure 7: Differential J/ψ meson cross sections for the kinematic range $3.6 < Q^2 < 100\,\mathrm{GeV}^2$, $60 < W_{\gamma p} < 240\,\mathrm{GeV}$, $0.3 < z < 0.9$ and $P^{*2}_{T,\psi} > 1\,\mathrm{GeV}$, as functions of a) the photon virtuality Q^2, b) the squared transverse momentum of the J/ψ meson in the photon proton rest frame $P^{*2}_{T,\psi}$, c) the energy in the photon proton rest frame $W_{\gamma p}$ and d) the elasticity z. The inner error bar represents the statistical uncertainty and the outer error bar indicates the statistical and systematic uncertainties added in quadrature. The data are compared to the predictions from CASCADE (solid line). The uncertainty band of the CASCADE prediction arises from a scale variation by a factor of two.

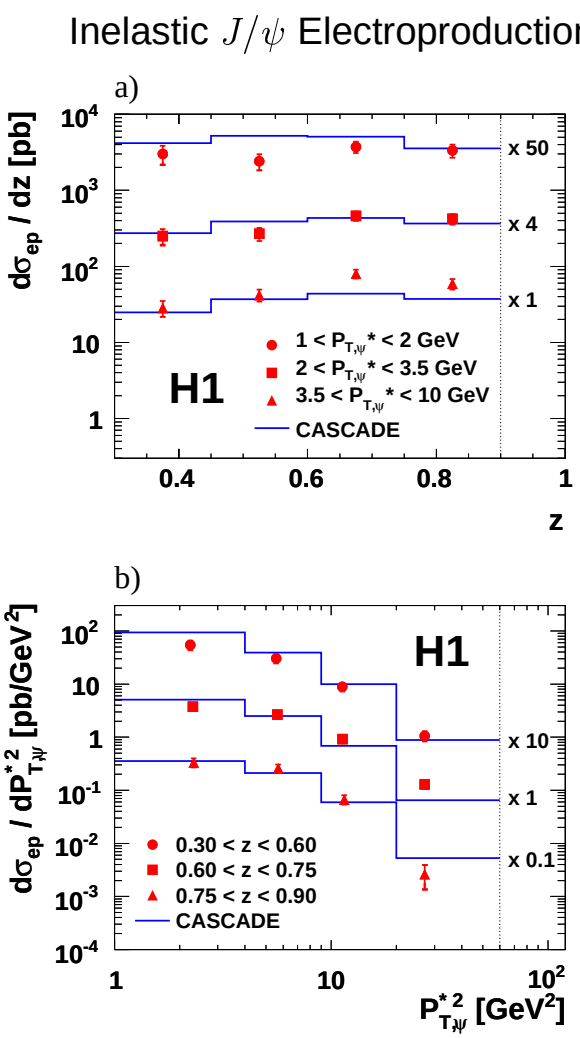

Figure 8: a) Differential J/ψ meson cross sections as a function of z in three bins of $P^*_{T,\psi}$ and b) differential cross section as a function of $P^{*2}_{T,\psi}$ in three bins of z. For visibility, the measured cross sections are scaled by the factors indicated in the figures. Predictions from CASCADE are shown as solid line.

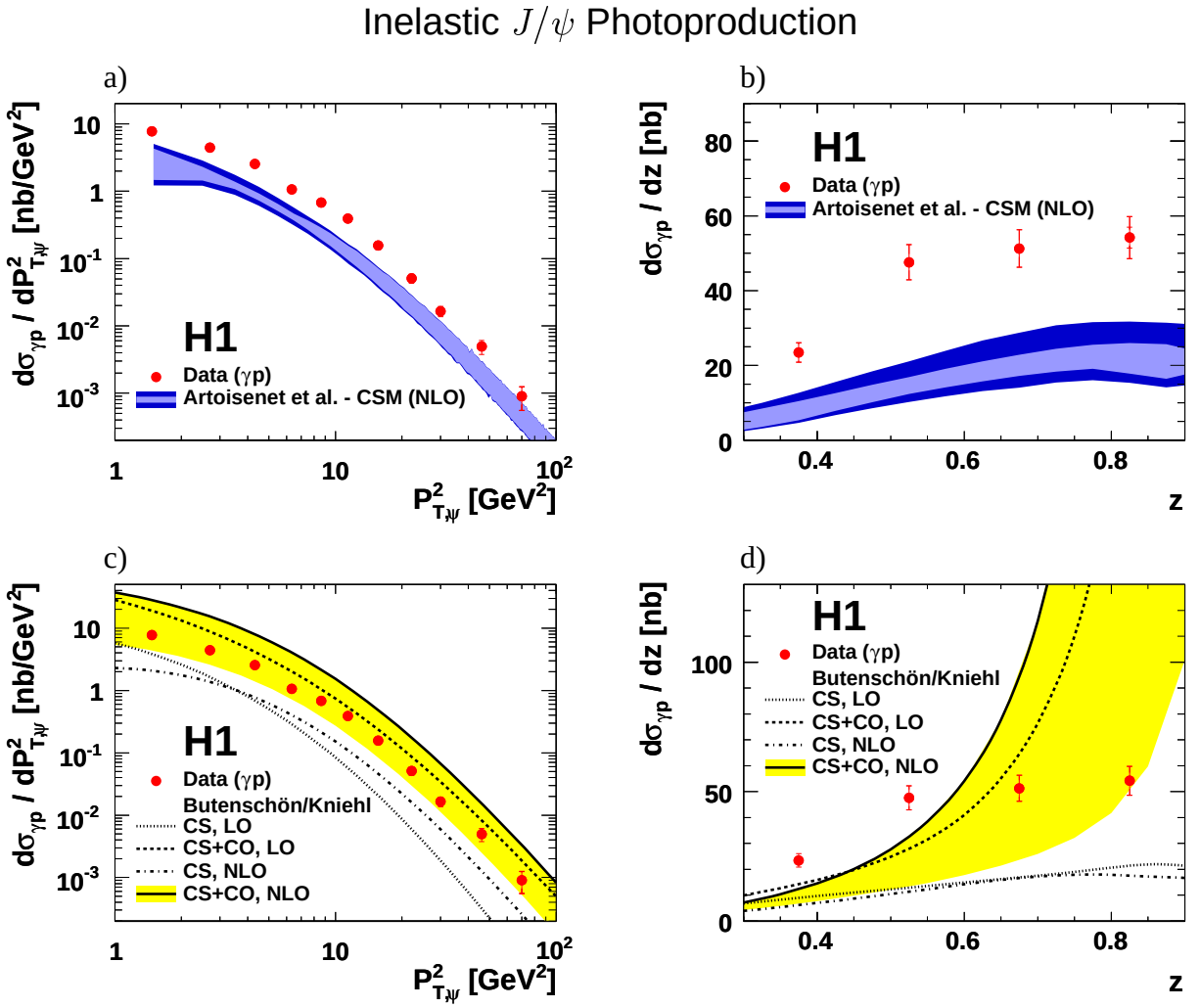

Figure 9: Differential J/ψ meson photoproduction cross sections for the kinematic range $60 < W_{\gamma p} < 240\,\mathrm{GeV}$, $0.3 < z < 0.9$ and $P_{T,\psi} > 1\,\mathrm{GeV}$ as functions of the squared transverse momentum of the J/ψ meson $P^2_{T,\psi}$ (a) and c)) and the elasticity z (b) and d)). The inner error bar represents the statistical uncertainty and the outer error bar indicates the statistical and systematic uncertainties added in quadrature. The data are compared with calculations to next-to-leading order: a,b) a colour singlet model (CSM) calculation [9] and c,d) a NRQCD calculation including contributions from colour octet states (CS + CO) [22]. The colour singlet component (CS) of the latter calculation is shown separately in addition.

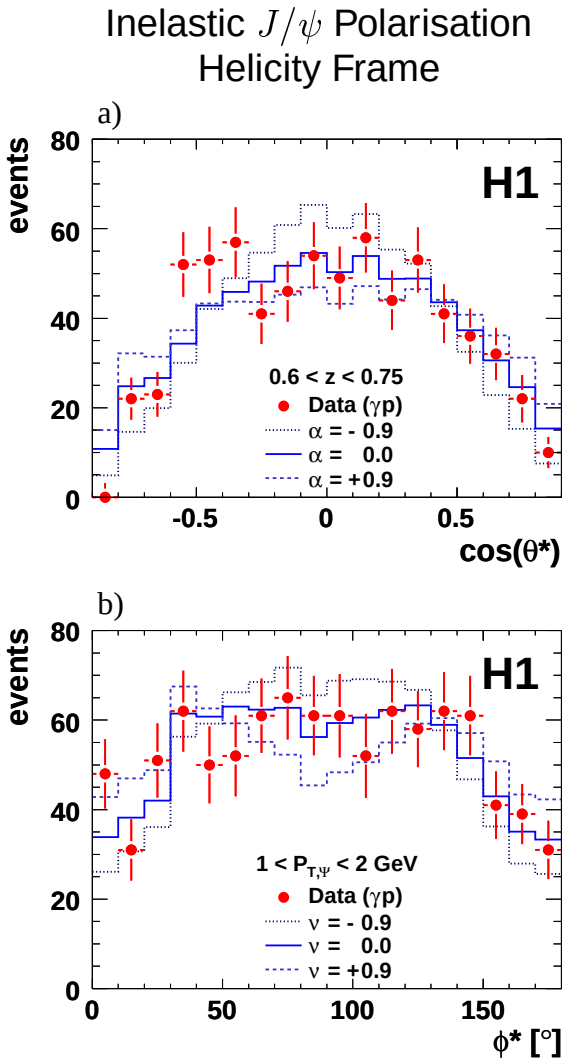

Figure 10: Distributions for a) $\cos(\theta^*)$ in the range $0.6 < z < 0.75$ and b) ϕ^* in the range $1 < P_{T,\psi} < 2\,\mathrm{GeV}$. The data are compared to the corrected CASCADE simulation with three different assumptions for the polarisation variables α or ν.

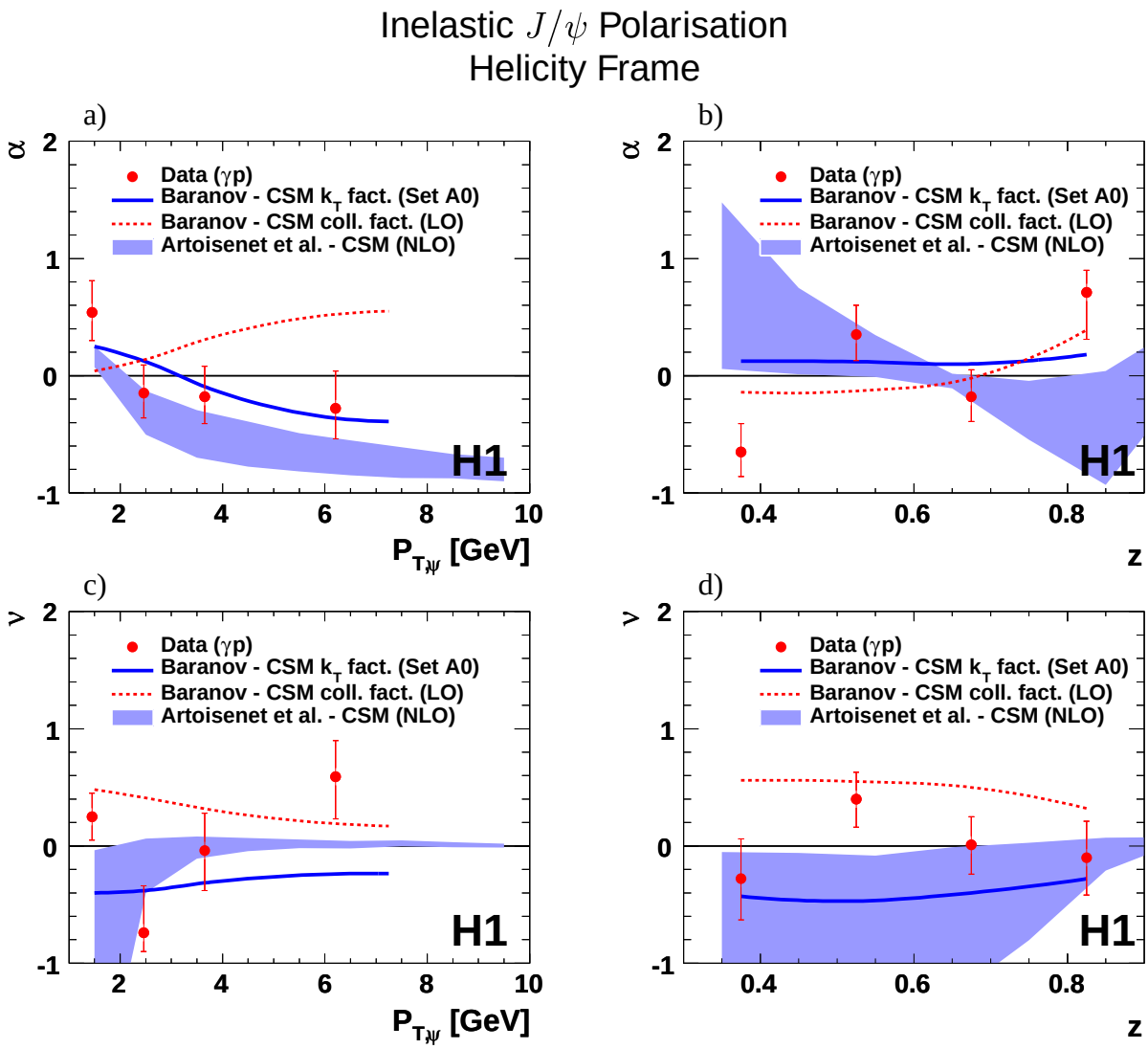

Figure 11: Polarisation parameters α and ν measured in the helicity frame for the kinematic range $60 < W_{\gamma p} < 240$ GeV, $0.3 < z < 0.9$ and $P_{T,\psi} > 1$ GeV, as a function of z and $P_{T,\psi}$. The measurement is compared with predictions calculated in a k_T factorisation ansatz [25] and with calculations in CSM (collinear factorisation) at leading [25] and next-to-leading order [9].

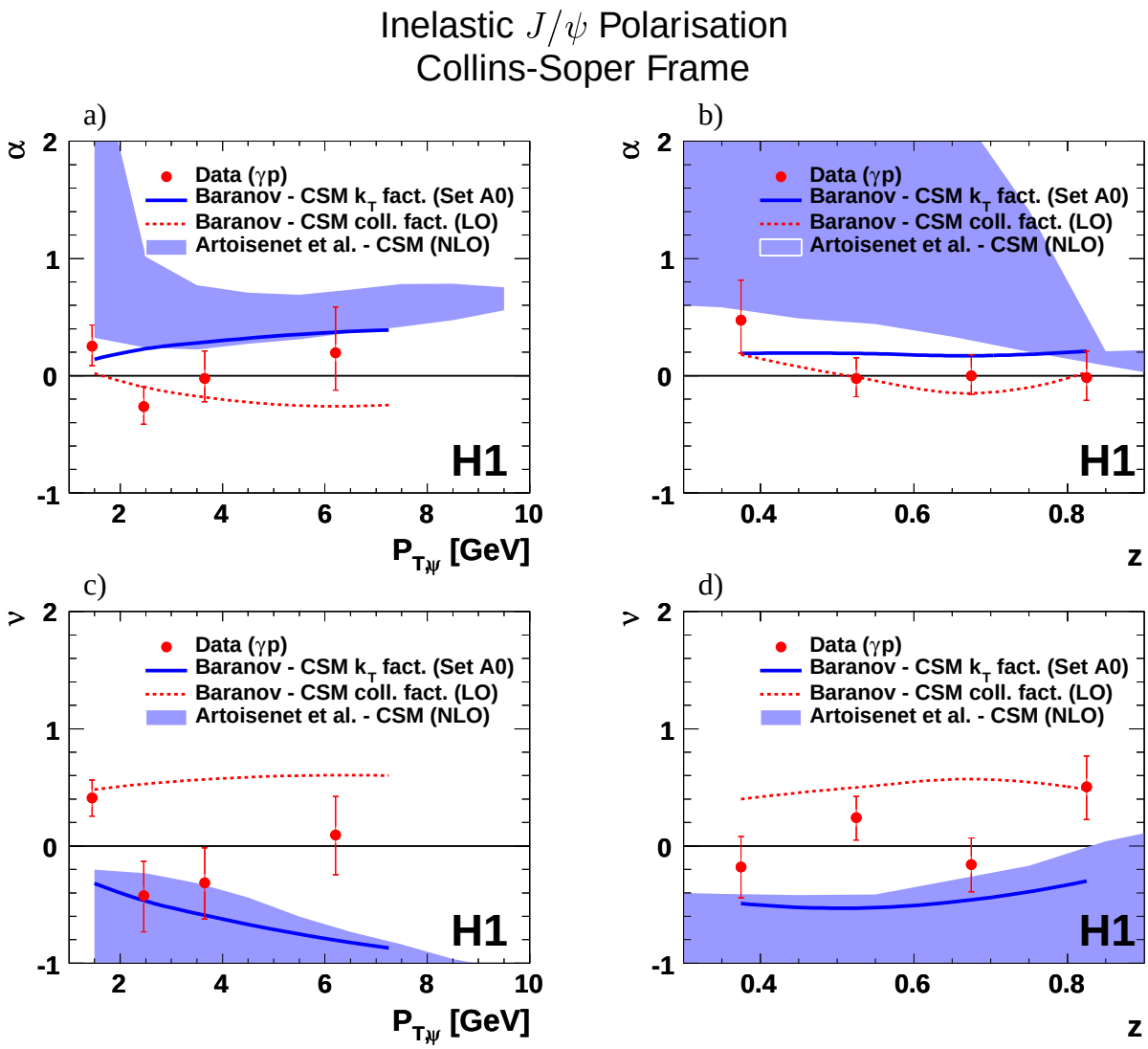

Figure 12: Polarisation parameters α and ν in the Collins-Soper frame for the kinematic range $60 < W_{\gamma p} < 240\,\mathrm{GeV}$, $0.3 < z < 0.9$ and $P_{T,\psi} > 1\,\mathrm{GeV}$, as a function of z and $P_{T,\psi}$. The measurement is compared with predictions calculated in a k_T factorisation ansatz [25] and with calculations in CSM (collinear factorisation) at leading [25] and next-to-leading order [9].

Inelastic J/ψ Photoproduction

$P^2_{T,\psi}$ [GeV^2]			$\langle P^2_{T,\psi} \rangle$ [GeV^2]	$\mathrm{d}\sigma_{\gamma\mathrm{p}}/\mathrm{d}P^2_{T,\psi}$ [nb/GeV^2]		
1.0	÷	2.1	1.5	7.75	± 0.82	± 0.70
2.1	÷	3.5	2.7	4.43	± 0.48	± 0.40
3.5	÷	5.4	4.3	2.55	± 0.28	± 0.23
5.4	÷	7.6	6.3	1.06	± 0.13	± 0.10
7.6	÷	10.0	8.6	0.677	± 0.084	± 0.061
10.0	÷	13.5	11.4	0.391	± 0.048	± 0.035
13.5	÷	20.0	15.6	0.156	± 0.020	± 0.014
20.0	÷	26.5	22.1	0.0509	± 0.0078	± 0.0046
26.5	÷	40.0	30.0	0.0175	± 0.0029	± 0.0015
40.0	÷	60.0	46.0	0.0049	± 0.0012	± 0.0004
60.0	÷	100.0	70.0	0.00090	± 0.00035	± 0.00008
z			$\langle z \rangle$	$\mathrm{d}\sigma_{\gamma\mathrm{p}}/\mathrm{d}z$ [nb]		
0.30	÷	0.45	0.375	23.4	± 2.6	± 2.1
0.45	÷	0.60	0.525	47.6	± 4.7	± 4.3
0.60	÷	0.75	0.675	51.3	± 5.0	± 4.6
0.75	÷	0.90	0.825	54.2	± 5.6	± 4.9

Table 4: Measured differential photoproduction cross sections in the kinematic range $0.3 < z < 0.9, P_{T,\psi} > 1\,\mathrm{GeV}$ and $60 < W_{\gamma p} < 240\,\mathrm{GeV}$ as function of the squared transverse momentum $P^2_{T,\psi}$ and the elasticity z of the J/ψ meson. The bin centre values, $\langle P^2_{T,\psi} \rangle$ and $\langle z \rangle$, are also given in the table.

Inelastic J/ψ Photoproduction

$W_{\gamma p}$ [GeV]			$\langle W_{\gamma p} \rangle$ [GeV]	Φ_γ	$\sigma_{\gamma\mathrm{p}}$ [nb]	
60	÷	80	69	0.0269	22.9 ± 4.1	± 2.1
80	÷	100	89	0.0192	24.1 ± 3.3	± 2.2
100	÷	120	110	0.0145	24.0 ± 3.0	± 2.2
120	÷	140	130	0.0112	30.3 ± 3.6	± 2.7
140	÷	160	150	0.00891	35.7 ± 4.3	± 3.2
160	÷	180	170	0.00716	30.4 ± 3.9	± 2.7
180	÷	210	194	0.00832	31.7 ± 4.2	± 2.9
210	÷	240	224	0.00621	33.8 ± 5.6	± 3.0

Table 5: Measured photoproduction cross sections in the kinematic range $P_{T,\psi} > 1\,\mathrm{GeV}$ and $0.3 < z < 0.9$ in bins of the photon proton centre-of-mass energy $W_{\gamma p}$. The bin centre values $\langle W_{\gamma p} \rangle$ are also given in the table. Φ_γ denotes the photon flux factors [52] employed in the photoproduction analysis using an upper Q^2 boundary of $Q^2 = 2.5\,\mathrm{GeV}^2$. For the range $60 < W_{\gamma p} < 240\,\mathrm{GeV}$ a photon flux factor of $\Phi_\gamma = 0.1024$ is calculated.

Inelastic J/ψ Photoproduction

$P^2_{T,\psi}$ [GeV^2]			$\langle P^2_{T,\psi} \rangle$ [GeV^2]	$\mathrm{d}\sigma_{\gamma\mathrm{p}}/\mathrm{d}P^2_{T,\psi}$ [nb/GeV^2]	
$0.30 < z < 0.45$					
1.0	÷	2.0	1.4	1.02	± 0.20 ± 0.09
2.0	÷	3.0	2.5	0.64	± 0.13 ± 0.06
3.0	÷	4.5	3.6	0.402	± 0.077 ± 0.036
4.5	÷	7.0	5.5	0.180	± 0.036 ± 0.016
7.0	÷	10.0	8.2	0.093	± 0.021 ± 0.008
10.0	÷	14.0	11.6	0.047	± 0.011 ± 0.004
14.0	÷	20.0	16.2	0.0210	± 0.0052 ± 0.0019
20.0	÷	40.0	25.0	0.0065	± 0.0018 ± 0.0006
40.0	÷	100.0	49.0	0.00065	± 0.00032 ± 0.00006
$0.45 < z < 0.60$					
1.0	÷	2.0	1.4	2.17	± 0.29 ± 0.19
2.0	÷	3.0	2.5	1.21	± 0.18 ± 0.11
3.0	÷	4.5	3.6	0.74	± 0.11 ± 0.07
4.5	÷	7.0	5.5	0.392	± 0.057 ± 0.035
7.0	÷	10.0	8.2	0.219	± 0.033 ± 0.020
10.0	÷	14.0	11.6	0.107	± 0.014 ± 0.010
14.0	÷	20.0	16.2	0.0497	± 0.0084 ± 0.0045
20.0	÷	40.0	25.0	0.0072	± 0.0015 ± 0.0007
40.0	÷	100.0	49.0	0.00072	± 0.00030 ± 0.00007
$0.60 < z < 0.75$					
1.0	÷	2.0	1.4	2.40	± 0.31 ± 0.22
2.0	÷	3.0	2.5	1.79	± 0.18 ± 0.11
3.0	÷	4.5	3.6	1.01	± 0.13 ± 0.09
4.5	÷	7.0	5.5	0.506	± 0.070 ± 0.046
7.0	÷	10.0	8.2	0.200	± 0.032 ± 0.018
10.0	÷	14.0	11.6	0.112	± 0.018 ± 0.010
14.0	÷	20.0	16.2	0.0413	± 0.0076 ± 0.0037
20.0	÷	40.0	25.0	0.0068	± 0.0014 ± 0.0006
$0.75 < z < 0.90$					
1.0	÷	2.0	1.4	2.40	± 0.36 ± 0.22
2.0	÷	3.0	2.5	1.69	± 0.27 ± 0.15
3.0	÷	4.5	3.6	0.86	± 0.15 ± 0.08
4.5	÷	7.0	5.5	0.437	± 0.076 ± 0.039
7.0	÷	10.0	8.2	0.226	± 0.042 ± 0.020
10.0	÷	14.0	11.6	0.099	± 0.022 ± 0.009
14.0	÷	20.0	16.2	0.0428	± 0.0098 ± 0.0039
20.0	÷	40.0	25.0	0.0076	± 0.0021 ± 0.0007

Table 6: Measured differential photoproduction cross sections in the kinematic range $0.3 < z < 0.9$ and $60 < W_{\gamma p} < 240\,\mathrm{GeV}$ as a function of the squared transverse momentum of the J/ψ meson in bins of the elasticity z. The bin centre values $\langle P^2_{T,\psi} \rangle$ are also given in the table.

Inelastic J/ψ Photoproduction

z			$\langle z \rangle$	$\mathrm{d}\sigma_{\gamma\mathrm{p}}/\mathrm{d}z$ [nb]	
$1.0 < P_{T,\psi} < 2.0\,\mathrm{GeV}$					
0.30	÷	0.45	0.375	14.9 ± 2.1	± 1.3
0.45	÷	0.60	0.525	28.3 ± 3.1	± 2.5
0.60	÷	0.75	0.675	31.8 ± 3.4	± 2.9
0.75	÷	0.90	0.825	33.6 ± 4.0	± 3.0
$2.0 < P_{T,\psi} < 3.0\,\mathrm{GeV}$					
0.30	÷	0.45	0.375	5.1 ± 0.8	± 0.5
0.45	÷	0.60	0.525	11.6 ± 1.4	± 1.0
0.60	÷	0.75	0.675	14.1 ± 1.6	± 1.3
0.75	÷	0.90	0.825	13.1 ± 1.8	± 1.2
$3.0 < P_{T,\psi} < 4.5\,\mathrm{GeV}$					
0.30	÷	0.45	0.375	2.60 ± 0.42	± 0.23
0.45	÷	0.60	0.525	6.05 ± 0.73	± 0.54
0.60	÷	0.75	0.675	5.71 ± 0.71	± 0.51
0.75	÷	0.90	0.825	5.32 ± 0.80	± 0.48
$P_{T,\psi} > 4.5\,\mathrm{GeV}$					
0.30	÷	0.45	0.375	1.10 ± 0.20	± 0.1
0.45	÷	0.60	0.525	1.30 ± 0.20	± 0.1
0.60	÷	0.75	0.675	1.11 ± 0.17	± 0.1
0.75	÷	0.90	0.825	1.30 ± 0.24	± 0.1

Table 7: Measured differential photoproduction cross sections in the kinematic range $P_{T,\psi} > 1\,\mathrm{GeV}$ and $60 < W_{\gamma p} < 240\,\mathrm{GeV}$ as a function of the elasticity z in bins of the transverse momentum of the J/ψ meson.

Inelastic J/ψ Electroproduction

Q^2 [GeV^2]			$\langle Q^2 \rangle$ [GeV^2]	$\mathrm{d}\sigma_{\mathrm{ep}}/\mathrm{d}Q^2$ [pb/GeV^2]		
3.6	÷	6.5	4.9	14.98	± 1.97	± 1.27
6.5	÷	12.0	8.6	6.33	± 0.75	± 0.54
12.0	÷	20.0	15.0	2.11	± 0.33	± 0.18
20.0	÷	40.0	26.7	0.74	± 0.12	± 0.06
40.0	÷	100.0	53.0	0.141	± 0.029	± 0.012
$P^{*2}_{T,\psi}$ [GeV^2]			$\langle P^{*2}_{T,\psi} \rangle$ [GeV^2]	$\mathrm{d}\sigma_{\mathrm{ep}}/\mathrm{d}P^{*2}_{T,\psi}$ [pb/GeV^2]		
1.0	÷	2.2	1.6	15.5	± 2.7	± 1.3
2.2	÷	3.7	2.9	11.0	± 2.1	± 0.9
3.7	÷	6.4	4.9	8.7	± 1.4	± 0.7
6.4	÷	9.6	7.8	5.90	± 0.92	± 0.50
9.6	÷	13.5	11.2	3.23	± 0.53	± 0.27
13.5	÷	20.0	16.0	1.69	± 0.27	± 0.14
20.0	÷	40.0	25.7	0.576	± 0.083	± 0.049
40.0	÷	100.0	51.0	0.055	± 0.012	± 0.005
z			$\langle z \rangle$	$\mathrm{d}\sigma_{\mathrm{ep}}/\mathrm{d}z$ [pb]		
0.30	÷	0.45	0.375	150	± 26	± 13
0.45	÷	0.60	0.525	158	± 22	± 14
0.60	÷	0.75	0.675	280	± 31	± 24
0.75	÷	0.90	0.825	239	± 29	± 20
$W_{\gamma p}$ [GeV]			$\langle W_{\gamma p} \rangle$ [GeV]	$\mathrm{d}\sigma_{\mathrm{ep}}/\mathrm{d}W_{\gamma p}$ [pb/GeV]		
60	÷	80	69	0.89	± 0.16	± 0.08
80	÷	100	89	1.03	± 0.15	± 0.09
100	÷	120	110	0.77	± 0.12	± 0.007
120	÷	140	130	0.75	± 0.11	± 0.06
140	÷	160	150	0.71	± 0.11	± 0.06
160	÷	180	170	0.55	± 0.10	± 0.05
180	÷	210	194	0.42	± 0.09	± 0.04
210	÷	240	224	0.30	± 0.10	± 0.03

Table 8: Measured differential electroproduction cross sections in the kinematic range $3.6 < Q^2 < 100\,\mathrm{GeV}^2$, $P^*_{T,\psi} > 1\,\mathrm{GeV}$ and $0.3 < z < 0.9$ as function of the four momentum transfer Q^2, the squared transverse momentum of the J/ψ meson in the photon proton rest frame $P^{*2}_{T,\psi}$, the elasticity z and the photon proton centre-of-mass energy $W_{\gamma p}$.

Inelastic J/ψ Electroproduction

$P^{*2}_{T,\psi}$ [GeV^2]			$\langle P^{*2}_{T,\psi} \rangle$ [GeV^2]	$\mathrm{d}\sigma_{\mathrm{ep}}/\mathrm{d}P^{*2}_{T,\psi}$ [nb/GeV^2]		
$0.30 < z < 0.60$						
1.0	$\div$	4.0	2.2	5.5	$\pm$ 1.1	$\pm$ 0.5
4.0	$\div$	9.0	5.6	3.0	$\pm$ 0.6	$\pm$ 0.3
9.0	$\div$	20.0	11.3	0.89	$\pm$ 0.17	$\pm$ 0.08
20.0	$\div$	60.0	27.0	0.11	$\pm$ 0.02	$\pm$ 0.01
$0.60 < z < 0.75$						
1.0	$\div$	4.0	2.3	3.7	$\pm$ 0.7	$\pm$ 0.3
4.0	$\div$	9.0	5.7	2.7	$\pm$ 0.4	$\pm$ 0.2
9.0	$\div$	20.0	11.3	0.92	$\pm$ 0.15	$\pm$ 0.08
20.0	$\div$	60.0	27.0	0.13	$\pm$ 0.03	$\pm$ 0.01
$0.75 < z < 0.90$						
1.0	$\div$	4.0	2.3	3.3	$\pm$ 0.7	$\pm$ 0.3
4.0	$\div$	9.0	5.7	2.6	$\pm$ 0.5	$\pm$ 0.2
9.0	$\div$	20.0	11.5	0.67	$\pm$ 0.13	$\pm$ 0.06
20.0	$\div$	60.0	27.0	0.026	$\pm$ 0.013	$\pm$ 0.002
z			$\langle z \rangle$	$\mathrm{d}\sigma_{\mathrm{ep}}/\mathrm{d}z$ [nb]		
$1.0 < P^*_{T,\psi} < 2.0\,\mathrm{GeV}$						
0.30	$\div$	0.45	0.375	60.0	$\pm$ 17.0	$\pm$ 5.1
0.45	$\div$	0.60	0.525	48.0	$\pm$ 11.4	$\pm$ 4.1
0.60	$\div$	0.75	0.675	74.6	$\pm$ 12.8	$\pm$ 6.3
0.75	$\div$	0.90	0.825	66.8	$\pm$ 12.9	$\pm$ 5.7
$2.0 < P^*_{T,\psi} < 3.5\,\mathrm{GeV}$						
0.30	$\div$	0.45	0.375	62.4	$\pm$ 15.1	$\pm$ 5.3
0.45	$\div$	0.60	0.525	67.1	$\pm$ 13.1	$\pm$ 5.7
0.60	$\div$	0.75	0.675	115.3	$\pm$ 16.2	$\pm$ 9.8
0.75	$\div$	0.90	0.825	105.0	$\pm$ 16.7	$\pm$ 8.9
$3.5 < P^*_{T,\psi} < 10.\,\mathrm{GeV}$						
0.30	$\div$	0.45	0.375	28.4	$\pm$ 6.7	$\pm$ 2.4
0.45	$\div$	0.60	0.525	41.9	$\pm$ 7.5	$\pm$ 3.6
0.60	$\div$	0.75	0.675	79.6	$\pm$ 10.6	$\pm$ 6.8
0.75	$\div$	0.90	0.825	58.9	$\pm$ 9.5	$\pm$ 5.0

Table 9: Measured differential electroproduction cross sections in the kinematic range $3.6 < Q^2 < 100\,\mathrm{GeV}^2, P^*_{T,\psi} > 1\,\mathrm{GeV}$ and $60 < W_{\gamma p} < 240\,\mathrm{GeV}$ as a function of the squared transverse momentum in the photon proton rest frame $P^{*2}_{T,\psi}$ in bins of the elasticity z and the elasticity z in bins of the transverse momentum in the photon proton rest frame $P^*_{T,\psi}$.

Inelastic J/ψ Photoproduction

Helicity Frame

$P_{T,\psi}$ [GeV]			$\langle P_{T,\psi} \rangle$ [GeV]	α	ν
1.0	$\div$	2.0	1.45	$+0.54\,^{+0.27}_{-0.24}$	$+0.25\,^{+0.20}_{-0.20}$
2.0	$\div$	3.0	2.46	$-0.15\,^{+0.24}_{-0.21}$	$-0.74\,^{+0.40}_{-0.16}$
3.0	$\div$	4.5	3.65	$-0.18\,^{+0.26}_{-0.23}$	$-0.04\,^{+0.32}_{-0.34}$
4.5	$\div$	10.0	6.21	$-0.28\,^{+0.32}_{-0.26}$	$+0.59\,^{+0.31}_{-0.36}$
z			$\langle z \rangle$	α	ν
0.30	$\div$	0.45	0.375	$-0.65\,^{+0.24}_{-0.21}$	$-0.28\,^{+0.34}_{-0.35}$
0.45	$\div$	0.60	0.525	$+0.35\,^{+0.25}_{-0.22}$	$+0.40\,^{+0.23}_{-0.24}$
0.60	$\div$	0.75	0.675	$-0.18\,^{+0.23}_{-0.21}$	$+0.01\,^{+0.24}_{-0.25}$
0.75	$\div$	0.90	0.825	$+0.71\,^{+0.19}_{-0.40}$	$-0.10\,^{+0.31}_{-0.32}$

Collins-Soper Frame

$P_{T,\psi}$ [GeV]			$\langle P_{T,\psi} \rangle$ [GeV]	α	ν
1.0	$\div$	2.0	1.45	$+0.25\,^{+0.18}_{-0.17}$	$+0.41\,^{+0.15}_{-0.16}$
2.0	$\div$	3.0	2.46	$-0.26\,^{+0.17}_{-0.15}$	$-0.42\,^{+0.29}_{-0.31}$
3.0	$\div$	4.5	3.65	$-0.02\,^{+0.23}_{-0.20}$	$-0.31\,^{+0.30}_{-0.31}$
4.5	$\div$	10.0	6.21	$+0.19\,^{+0.39}_{-0.32}$	$+0.09\,^{+0.33}_{-0.34}$
z			$\langle z \rangle$	α	ν
0.30	$\div$	0.45	0.375	$+0.47\,^{+0.34}_{-0.28}$	$-0.18\,^{+0.26}_{-0.26}$
0.45	$\div$	0.60	0.525	$-0.02\,^{+0.18}_{-0.16}$	$+0.24\,^{+0.18}_{-0.19}$
0.60	$\div$	0.75	0.675	$-0.00\,^{+0.18}_{-0.16}$	$-0.16\,^{+0.23}_{-0.23}$
0.75	$\div$	0.90	0.825	$-0.02\,^{+0.23}_{-0.19}$	$+0.50\,^{+0.26}_{-0.28}$

Table 10: Measured polarisation parameters in the helicity and the Collins-Soper frame as function of $P_{T,\psi}$ and z in the kinematic range $P_{T,\psi} > 1\,\mathrm{GeV}, 60 < W_{\gamma p} < 240\,\mathrm{GeV}$ and $0.3 < z < 0.9$.